



SAPIENZA
UNIVERSITÀ DI ROMA

Beam injection optimization in the SPARC_LAB plasma accelerator

Facoltà di Scienze Matematiche Fisiche e Naturali

Corso di laurea in Fisica

Candidato Michele Croia

n° matricola 1104662

Relatore

Prof. Riccardo Faccini

Correlatore

Dott. Massimo Ferrario

A/A 2013/2014

“Solo lo stupore conosce”

M.Bersanelli

Contents	v
Introduction	1
1 The Sparc_Lab facility	5
1.1 Introduction to SPARC_LAB	5
1.2 Linac layout: electron gun and accelerating structures ..	6
1.2.1 Laser Flame	8
1.2.2 Photo-cathode laser System	10
1.2.3 Linac upgrade: C-band	12
1.3 Thomson back-scattering source	15
1.4 THz source	17
1.5 Free Electron Laser	18
1.6 Plasma acceleration experiment at SPARC_LAB	21
2 Beam dynamics	25
2.1 Particle accelerator	25
2.2 Limits for traditional accelerators	28
2.3 Basic principles on beam focusing and transport	30
2.3.1 Laminar and non-laminar beams	30
2.3.2 The emittance concept	34
2.3.3 The rms envelope equation	40
2.3.4 External forces	45
2.3.5 Space charge forces	47
2.4 Production of ultrashort electron bunches with low emittance	53
3 Plasma Acceleration	57
3.1 Principles of plasma acceleration	59
3.2 Laser Driven Plasma Accelerators	62
3.3 Beam Driven Plasma Accelerarors	66
3.3.1 Regimes in a PWFA	68
3.3.2 Matching conditions in a Plasma Accelerator	71
3.4 Chapter conclusions	79

4	Numerical simulations	81
4.1	General Particle Tracer (GPT)	81
4.2	The GPT executable	83
4.3	Linac start to end simulation	86
4.4	Ultrashort and low emittance bunch simulation	88
4.5	The COMB interaction chamber	93
4.6	Matching conditions at SPARC_LAB	95
4.7	Insertion of magnetic elements before plasma	97
4.8	Final results for the spot size	100
4.9	Regime for the COMB experiment	102
4.10	Plasma like a THz cavity	104
5	Conclusions	107
	Bibliography	111
	Ringraziamenti	119

Introduction

Particle accelerators are used in many fields of science. Historically they were developed for nuclear and, then, for particle physics research. In both cases, the growing demand in terms of energy, power and beam current required ever more complex machines with the aim to achieve the maximum allowed accelerating gradient, i.e. the maximum energy gained by a particle in a fixed length. The strength of the maximum electric field available in state of the art particle accelerators using radio-frequency (RF) technology is limited to about 150 MV/m at most. Therefore, increasing the length of the accelerator is the only way to reach higher energies. This is why nowadays accelerators are many kilometers in size with little potential for further increases in energy. In addition to nuclear and particle physics during the years particle accelerators became widely used as advanced radiation sources to produce light in a spectrum going from sub-millimeters (THz radiation) to nanometres wavelengths produced by Free Electron Lasers, representing a powerful tool, e.g. for condensed matter physics, molecular biology, chemistry, material science and medicine. Free Electron Lasers (FEL), in particular, are capable to produce high brilliance light with wavelengths up to several Angstroms and in very short pulses, allowing time resolved measurements like femto-chemistry, which studies chemical reactions on extremely short timescales, approximately 10^{-15} seconds (one femtosecond). Nevertheless, high energy beams are needed also for FELs in order to reach the very short wavelengths.

The actual and common demand is therefore to have higher energies particles accelerated in less space. In this sense, the new technique which seems to attract the main efforts is based on plasma accelerators. In a

plasma accelerator, the role of the accelerating structure is played by the plasma, an ionized gas, and the power source is not microwave (RF) radiation but is either a laser beam or a charged particle beam. As a result, plasma waves exert accelerating gradients of several tens of GV/m. The accelerating gradient can be enhanced by "simply" increasing the plasma density n_0 .

The length moves therefore from the tens of meters scale of conventional RF accelerators to a centimeter scale. Despite this, the main issue related to plasma accelerators is the high energy spread (of the order of 10%) in the accelerated beam if compared with conventional machines (about 0.1%). It is due to the fact that the plasma wavelength λ_p is microscopic, about $330 \mu m$ for plasma densities of $10^{16} cm^{-3}$ (while RF waves are about $10 cm$ long), therefore particles must be injected in such a small structure and in correspondence of the accelerating region. This leads to focus the attention on methods capable to increase the accelerated beam quality at the level of conventional accelerators. Actually the most promising plasma technique is the Plasma Wakefield Acceleration (PWFA), in which the plasma wave is generated by an externally injected electron beam produced by a conventional RF photo-injector.

At SPARC_LAB facility located in Frascati a PWFA experiment named COMB have been proposed and it will start in the 2015, in this experiment a train of electron bunches will be injected in a plasma capillary of $5 cm$. This bunches will be spaced by one λ_p with dimensions less to $\lambda_p/2$.

In my thesis work I evaluated the focusing elements on the beam line to achieve, in the SPARC_LAB linac, the best spot size to start the COMB plasma acceleration experiment.

After an introduction to the SPARC_LAB facility (Chapter 1), Chapter 2 presents the beam dynamics theory and the beam envelope equation. Chapter 3 is an overview of the plasma acceleration in both the configurations Laser Wakefield Acceleration (LWFA) and PWFA, focalizing the attention on the beam driven configuration. Chapter 3 describes a simple model to estimate the matching conditions between plasma and electron bunch in PWFA.

During this thesis work in order to obtain the matching conditions in the COMB experiment was simulated the SPARC_LAB linac, from start to end, and the COMB interaction chamber, searching for an optimised scheme of the focusing magnetic elements in the beam line and inserting two new triplets of quadrupoles before plasma. The software used for this simulations is General Particle Tracer (GPT) and it will presented in Chapter 4, for data analysis both GPT and the software MATLAB have been used.

Chapter 4 describes the impact of the results inserting in the beam line this two new triplets of quadrupoles and using the SPARC_LAB S2-solenoid with a proper current. With this configuration we will achieve the spot size at SPARC_LAB suitable for the COMB experiment.

Afterwards a simulation in which the plasma, with a density of $n_0 = 10^{16}$, was performed with GPT by assuming the plasma wake like an accelerating section with a frequency of $1 THz$. With this simulation were grossly evaluated the gradients of three quadrupoles after plasma, in order to capture the bunch after the plasma acceleration.

Chapter 1

The SPARC_LAB facility

This chapter describes the facility SPARC_LAB (LNF - INFN, Frascati), consisting in a 5.6 MeV electron gun followed by three travelling wave (TW) sections, providing beam energies up to 180 MeV for four experimental beam lines. After an introduction to the facility, the experiments installed in the facility are shortly described.

1.1 Introduction to SPARC_LAB

The facility SPARC_LAB (Sources for Plasma Accelerators and Radiation Compton with Lasers and Beams) is located at the INFN National Laboratories in Frascati. It is based on the unique combination of high brightness electron beams, from the SPARC photoinjector [1, 2], with high intensity ultrashort laser pulses from FLAME [3], a 200 TW laser that is linked to the linac. The joint presence of these two systems allows the investigation of plasma acceleration with different configurations, i.e. self and external injection, laser and particle beam driven. In addition, the development of a wide spectrum inter-disciplinary leading-edge research activity based on advanced radiation sources, e.g. Free Electron Laser (FEL) experiments in SASE, Seeded and new configurations [4, 5, 6], the production of X-rays by means of Thomson back-scattering [7, 8] and high peak power THz radiation, both broadband [9] and narrowband [10] are studied. An upgrade of the linac is also foreseen by the end of 2014 by

installing one new high gradient C-band structures. The Figure 1.1 shows the linac layout and the four beam lines.



Figure 1.1: SPARC_LAB layout. The electron-gun (1) followed by the three TW accelerating sections (2). Vice the third section (4) there will be a new C-band, and a PWFA experiment (3); these are then followed by the first dipole (5). Four beam lines follows the dipole, devoted to FEL physics (6) both in SASE and seeded (6b) schemes, beam diagnostics (7) based on EOS and THz radiation, plasma acceleration by LWFA (8), and X-rays production in the Thomson interaction chamber (9) by colliding the electron beam with the FLAME laser (10). The EOS laser comes from the photo-cathode laser room (11) and is delivered to the EOS station by using the EOS transfer line (12).

1.2 Linac layout: electron gun and accelerating structures

The SPARC_LAB photo-injector is shown in Figure 1.2. It is composed by a 1.6 cell BNL/UCLA/SLAC type gun, operating at S-band (2.856 GHz) with high peak field (120 MV/m) on the incorporated metallic photocathode (Cu), generating a 5.6 MeV electron beam with a quantum efficiency in typical conditions of about few 10^{-5} . The gun is then followed by three 3 m

long S-band travelling wave (TW) sections (hereinafter called S1, S2 and S3) whose accelerating gradient ($< 25MV/m$) boosts the beam energy up to 180 MeV. The first one is also used as RF compressor (velocity bunching regime) by varying the beam injection phase. Solenoid coils embedding the first two sections can be powered to provide additional magnetic focusing to better control the beam envelope and the emittance oscillations under RF compression. A diagnostics transfer line allows to fully characterize the accelerated beam by measuring transverse emittance [11], longitudinal profile, and slice emittance through a Radio-Frequency Deflector (RFD) [12]. The current layout follows a detailed theoretical study of the emittance compensation process in a photoinjector [13]. It has been demonstrated that the best optimization is achieved by propagating the beam through the device so that emittance oscillations produced by space charge collective forces are damped while the beam is accelerating [14]; the basic point in the design of a photo-injector is therefore the properly match of the beam from the injector to the accelerating sections. In fact, being the brightness a figure of merit defined as [15]:

$$B = \frac{2I}{\pi^2 \varepsilon_{n,x} \varepsilon_{n,y}} \quad (1.1)$$

where I is the beam current and $\varepsilon_{n,x,y}$ is the normalized emittance, to increase the brightness high current and small emittance beams are required. It has been predicted [16] and then measured [17] that the proper tuning of the emittance oscillation can be achieved by injecting the beam into the linac when the emittance reaches its relative maximum. By using the SPARC_LAB gun, it is located at a distance of 1.5 m, in this case the second emittance minimum is moved to the linac output, allowing to obtain

high brightness and low emittance beams. This working point is called Ferrario's working point and it is widely used in photo-injectors.



Figure 1.2: The SPARC_LAB photo-injector. The electron gun, providing a 5.6 MeV beam energy, is followed by three TW accelerating sections (S1, S2 and S3), with the first two having solenoid coils embedded.

1.2.1 Laser Flame

The SPARC_LAB high power laser system is named FLAME, it is based upon a Ti:Sa, chirped pulse amplification (CPA) laser able to deliver up to 220 TW laser pulses, 25 fs long, with a 10 Hz repetition rate at a fundamental wavelength of 800 nm , see Figure 1.3.

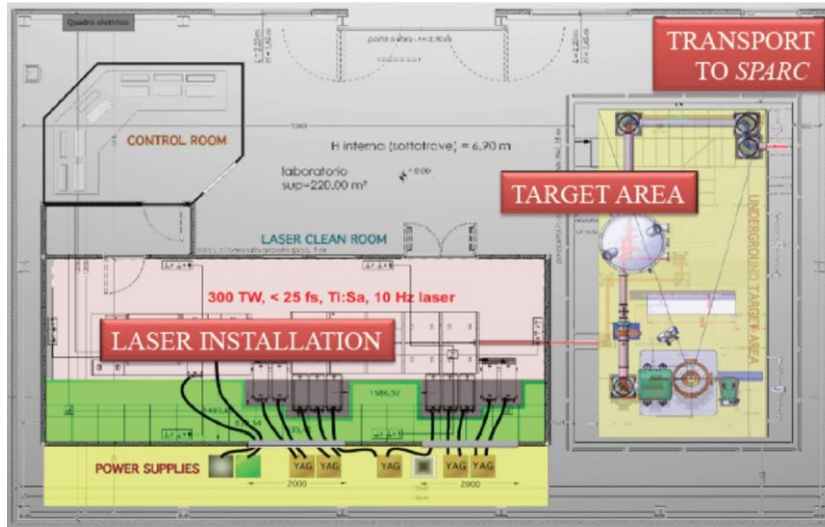


Figure 1.3: Layout of the FLAME laser with the target area for self-injection plasma acceleration experiments

The system features are characterized by a high contrast ratio ($> 10^{10}$) and a fully remotely controlled operation mode. It includes a front-end with pulse contrast enhancement, bandwidth control and regenerative amplifier and yields pulses with 0.7 mJ in 80 nm bandwidth. These pulses are then further amplified by the first amplifier up to 25 mJ while the second amplifier brings the energy up to 600 mJ . The third cryogenic amplifier is based on a 50 mm Ti:Sa crystal pumped by 10 frequency doubled Nd:YAG laser pulses, reaching an energy up to 20 J at 532 nm . The extraction energy is as high as 35%, leading to a final energy in the stretched pulses in excess of 7 J . The pulse is then compressed to minimum pulse duration below 30 fs . Once compressed, the pulse is transported under vacuum to the target area via remotely controlled beam steering mirrors. For typical experimental conditions of laser wakefield acceleration in self-injection configuration, the laser pulse is focused at peak intensities exceeding 10^{18} W/cm^2 which, with our ASE contrast, gives a precursor laser intensity on a target below 10^9 W/cm^2 . In the case of interaction with gases at

pressures ranging from 1 to 10 *bar*, this laser intensity is below the plasma formation threshold for laser pulses of sub-nanosecond duration, which is typical duration of the ASE pulses. Therefore, we can reasonably assume that, in the case of interaction with gases, no premature plasma formation occurs and the CPA pulse can be focused directly in the gas.

Among the different uses of FLAME there are: self-injection and external injection [18] experiments and an X-ray source based on the Thomson backscattering process. To this purpose, a careful characterization of FLAME performances with particular reference to the transverse beam quality was carried out during the commissioning. The measured Strehl ratio is greater than 50% up to pulse energies of approximately 6 *J*. For energies between 6 and 7 *J*, the phase front distortion increases leading to the reduction of the Strehl ratio to a minimum value of 35%. Measurements show that the phase front pattern remains very stable from shot to shot at a given pulse energy. This makes the phase front correction with adaptive optics a reliable and complete solution to achieve a high quality focal spot.

1.2.2 Photo-cathode laser System

The SPARC_LAB photocathode laser [19], operating in single pulse mode at 10 *Hz* repetition rate, is a Ti:Sapphire system manufactured by Coherent™. The laser (see Figure 1.4) consists of a Ti:Sa oscillator which generates 50 *fs* (*rms*) pulses synchronized with the 2856 *MHz* accelerating field of the linac, within about 1° *rms* (0.973 *ps*). The oscillator operates at a repetition rate of 79.3 *MHz* corresponding to the 36th sub-harmonics of the RF-frequency. It is pumped by the 2nd harmonic of a Nd:YVO₄ laser (Verdi by Coherent™). This laser delivers 5 *W* CW power at 532 *nm*. The laser amplification process is carried out by a regenerative preamplifier pumped

by a 10 W Nd:YLF laser and by two double pass stages excited by the 2nd harmonic of a Nd:YAG with an energy of 0.5 J per pulse. It delivers pulses at $\lambda = 800 \text{ nm}$ with energy up to 50 mJ and a repetition rate of 10 Hz.

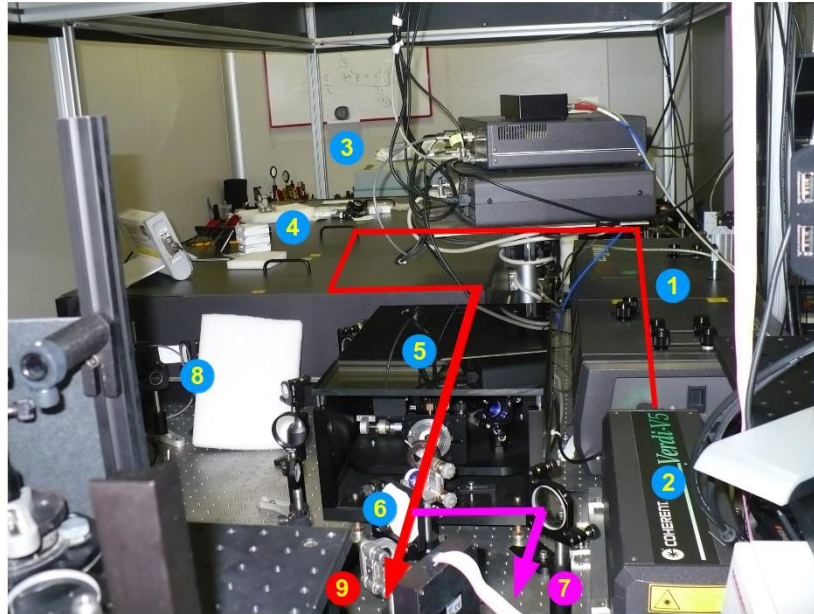


Figure 1.4: Schematic layout of the laser system, composed by a Ti:Sa oscillator (1) pumped by a Nd:YVO₄ (2) followed by a Nd:YAG pump (3) and the CPA system (4). The IR laser then enters into the 3rd harmonic generator (5) to produce UV light. An UV-coated mirror (6) then reflects the UV light (7), that can be send directly to the photo-cathode or shaped by an UV stretcher (8), while transmitting the IR light (9) that is carried up to the EOS vacuum chamber.

After the amplifier the IR pulses enter a 3rd harmonic generator producing about 60 fs (rms) long UV pulses with an energy up to 3 mJ. The frequency upconversion is required to generate photons with energies larger than the work function of the photo-cathode. A threshold of 4.59 eV for copper is quoted in the literature [20]. The Schottky effect reduces (at 30° from the rf phase zero crossing) the work function in operating conditions to 4.3 eV. The photon energy is 4.66 eV (corresponding to a 266.7 nm wavelength)

obtained as the third harmonic of 800 nm by using a system consisting of two β -cut beta barium borate (β -BBO) crystals of 0.5 and 0.3 mm thickness: the system produces the 2nd harmonic signal and then the 3rd harmonic one, at 266 nm , by frequency sum. This stage is followed by a switch that can send the laser pulse in an UV stretcher to lengthen the pulse up to 15 ps . Then the UV laser can be sent directly to the photo-cathode or, if it has not been stretched, to the laser-comb system composed by an half wave plate and an α -cut beta barium borate (α -BBO) birefringent crystal.

At this point, both UV light and residual IR light (that has not been converted in UV) are present; an UV-coated mirror reflects the UV light into an optical transfer line that is used to create the beam image on the cathode while the IR light is transmitted to an IR-coated mirror that sends the residual IR to the EOS transfer line, delivering it up to the EOS vacuum chamber.

1.2.3 Linac upgrade: C-band

At the end of 2014 there will be an upgrade of the actual linac by installing two new high gradient C-band TW structures in place of S3. This new sections have a double frequency $f = 5712\text{ MHz}$ compared to S3 $f = 2856\text{ MHz}$, and are able to achieve an accelerating field as high as 35 MV/m ; each structure is 1.4 m long. The new C-band structures are fed by a 50 MW klystron Toshiba E37202. The high voltage pulsed modulator and the 400 W solid state driver for the klystron have been manufactured respectively by ScandiNova (S) and MitecTelecom (CDN). The new system will also include a pulse compressor provided by the Institute of High Energy Physics (IHEP, Beijing). The mechanical drawing of the prototype is

given in Figure 1.5, Table 1.1 reports the main structure parameters and the mechanical drawings of the single cell are shown in Figure 1.6.

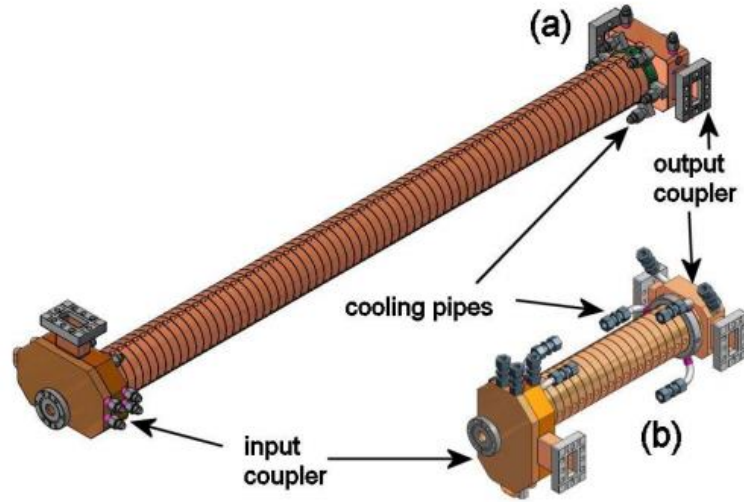


Figure 1.5: Mechanical drawing of the C-Band Structure (a) and prototype (b). Picture taken from [21].

PARAMETER	Value
Frequency (f_{RF})	5.712 [GHz]
Phase advance per cell	$2\pi/3$
Number of accelerating cells (N)	71
Structure length including couplers (L)	1.4 [m]
Cell length (d)	17.495 [mm]
Iris radius (a)	7 [mm]
Group velocity (v_g/c):	0.0283
Field attenuation (α)	0.206 [1/m]
Shunt impedance (r)	82.8 [M Ω /m]
Filling time (τ_F)	150 [ns]
Accelerating gradient	>35 [MV/m]
Output power	0.60 \cdot P _{in}
Average dissipated power @ 10 Hz	59.6 [W]

Table 1.1: Main C-Band structure parameters

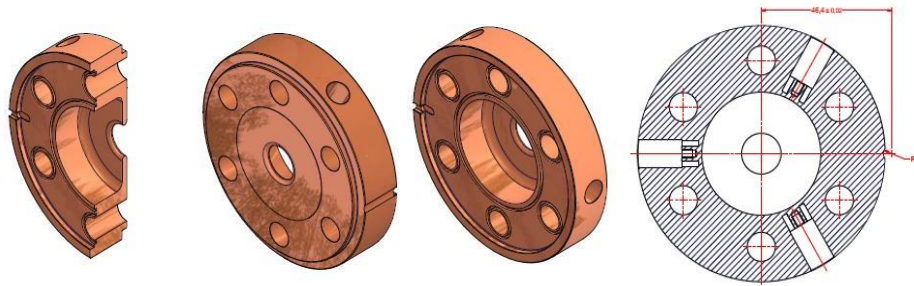


Figure 1.6: Mechanical drawings of the single cell.

Every structure is composed by two stacks with a central junction, this C-band can reach an accelerating field of $50\text{MV}/\text{m}$. The first structure has been installed in the SPARC hall for high power test, see Figure 1.7

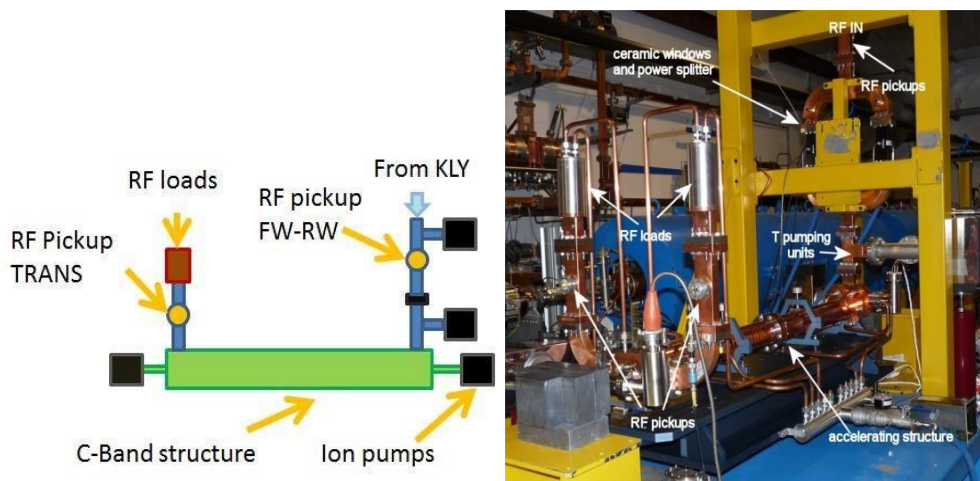


Figure 1.7: C-Band structure installed in SPARC for high power tests.

The compactness of the C-band structure is also a fundamental feature for the COMB experiment. In fact the possibility to replace, in the available room, the second C-band structure with the COMB interaction chamber while keeping a beam energy as high as 180 MeV will give more available energy to the drive beam for the plasma experiments.

1.3 Thomson back-scattering source

In the fourth line at Sparc_Lab there is a Thomson back-scattering X-ray source, it is able to work in three different operating modes: the high-flux-moderate-monochromaticity-mode (HFM2), suitable for medical imaging, the moderateflux-monochromatic-mode (MFM) suitable to improve the detection/dose performance [22, 23] and the shortand-monochromatic-mode (SM) useful for pump-andprobe experiments e.g. in physical-chemistry when tens of femtosecond long monochromatic pulses are needed.

The beamline have a transfer line for the electron beam together with a photon beamline that brings the laser pulse from FLAME target area to the interaction with the electron beam. In this configuration the electron beam energy can range from 28 MeV up to 150 MeV , and the electron beam transport is meant to preserve the high brightness coming from the linac and to ensure a very tight focusing and a longitudinal phase space optimization for the whole energy span. The general layout is shown in Figure 1.1, where the electron transfer line departs from a three way vacuum chamber inside the first dipole downstream the RF deflector that is used for the six-dimensional phase space analysis of the electron beam.

The electron beamline consists in a 30 m double dogleg starting, as mentioned, downstream the SPARC photoinjector; they ends in a two branch beam delivery line that provides two separate interaction regions with the possibility to host two different experiments at the same time: the Thomson source and the external injection in a plasma accelerator experiment.

The Thomson interaction vacuum chamber, see Figure 1.8, consists in two mirror stations that determine the in and out trajectory of the photon beam,

plus an interaction chamber in the middle that hosts the diagnostic for both the electron and photon beams. The parabolic mirror located downstream the interaction point focuses the photon beam at the interaction point down to a $10\ \mu\text{m}$ spot size, its spatial adjustment is obtained with its x-y movable support that can be also remotely controlled. The interaction chamber is a tee-vacuum chamber where a double screen movement is mounted to get the imaging of the electron and photon beam at the interaction point.

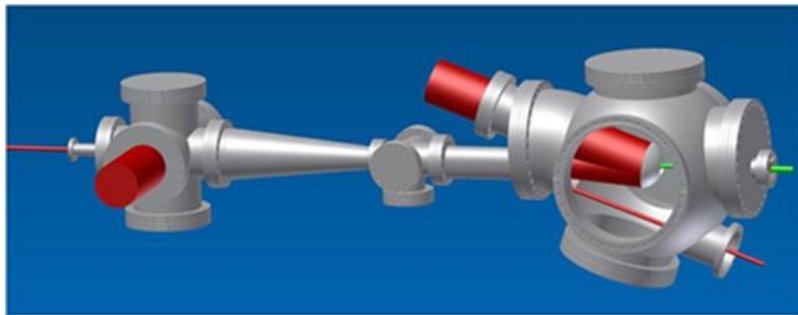


Figure 1.8: Drawing of the Thomson scattering interaction chamber.

The laser beam transfer line to the interaction region is composed by a series of high reflectivity mirrors inserted in a vacuum pipe $50\ \text{m}$ long. The mirrors, 8 inches diameter, are supported by motorized gimbal mounts in order to assure the alignment up to the off-axis parabola that focus the laser pulse on the electron beam. The vacuum of the photon beam line is at the level of 10^{-6} Torr.

The Thomson scattering experiment needs an extremely precise synchronization between electron bunch and laser pulse. The relative time of arrival jitter of the two beams is fundamental to obtain a repeatable and efficient interaction. The electrons and photons have to be synchronized with a relative jitter $< 500\ \text{fs}$. This can be obtained with a standard electrical distribution of the reference signal. Anyway an optical distribution

is preferable to obtain precise time of arrival measurement resolution (equal or less than $5fs$) and to obtain better synchronization between the two beams, a necessary requirement for the external injection in the plasma accelerator experiments. This can be achieved by means of an optical crosscorrelation between short laser pulses ($100 - 200 fs$). In particular the electrical (or optical) master oscillator in this project serves two laser oscillator clients: the photo injector laser for the production of electrons and the FLAME laser.

1.4 THz source

The motivation for developing a linac-based THz source at SPARC_LAB stays in the ever growing interest of filling the so-called THz gap with high peak power radiation. From simulations, the peak power expected at SPARC is in the order of $10^8 W$. This result has been confirmed by measurements presented in [24]. The corresponding energy per pulse is of the order of tens of μJ that is well above standard table top THz sources.

Applications of this kind of source concern mainly time domain THz spectroscopy and frequency domain measurements on novel materials [25]. Beyond these applications, coherent THz radiation is also used as longitudinal electron beam diagnostics to reconstruct the beam charge distribution [26].

In addition, taking advantage from electron beam manipulation techniques, high power, narrow-band THz radiation can be also generated at SPARC_LAB. This provides a unique chance to realize, with the SPARC THz source, THz-pump/THz-probe spectroscopy, a technique practically unexplored up to now.

The source is both Coherent Transition Radiation (CTR) from an aluminium coated silicon screen and Coherent Diffraction Radiation (CDR) from a rectangular cut on the screen. The screen is placed in the vacuum pipe at the end of the by-pass, at 45° with respect to the electron beam direction. Two branches are installed: one for interferometer measurements and one for integrated CTR/CDR measurements with the possibility of selecting custom band pass filters in the *THz* range.

CTR/CDR is emitted by both an ultrashort high-brightness electron beam and a longitudinally modulated one, based on the combination of velocity bunching and laser comb techniques. Depending on the working point of the accelerator, the *THz* radiation can be tuned in order to optimize different characteristics. So far achieved *THz* radiation performances, through CTR generated by a single bunch (500 pC, 500 fs with 110 MeV energy) are reported in Table 1.2.

Energy per pulse (μJ)	~ 10
Peak power (MW)	100
Average power (W)	2×10^{-4}
Electric field (kV/cm)	> 100
Pulse duration (fs)	< 200

Table 1.2. THz source achieved performances

1.5 Free Electron Laser

In a conventional laser the average output power is limited by how much of the unused power (which is significantly larger than the output power) that can be dissipated by the active medium. Moreover the light from a laser is seldom diffraction limited owing to heat effects in the lasing medium and non-linear processes taking place in the medium.

Contrasting this is the free electron laser process which can be close to unity in efficiency. In a free electron laser the amplification of the electromagnetic field occurs by the interaction between an electron beam and the radiation field it creates when moving through a periodic magnetic structure. Hence the operating wavelength is tunable via machine parameters such as electron beam energy, and magnetic field strength [27]. The resulting wavelength is:

$$\lambda = \frac{\lambda_u}{2\gamma^2} \left(1 + \frac{K^2}{2} \right) \quad (1.2)$$

where λ_u is the undulator period and $K \approx 0.9337B_0\lambda_u$ is a non-dimensional parameter, with the magnetic field B_0 measured in *Tesla* and undulator period in centimeters.

There is a number of free electron lasers operating in the world today, covering light wavelengths from the infrared to the X-ray regions; they have unprecedented beam properties and are currently the most intense and well collimated man-made photon source in the UV to the hard X-ray range. Free Electron Lasers have a lot experimental applications with an equally broad and diverse user community from many different fields.

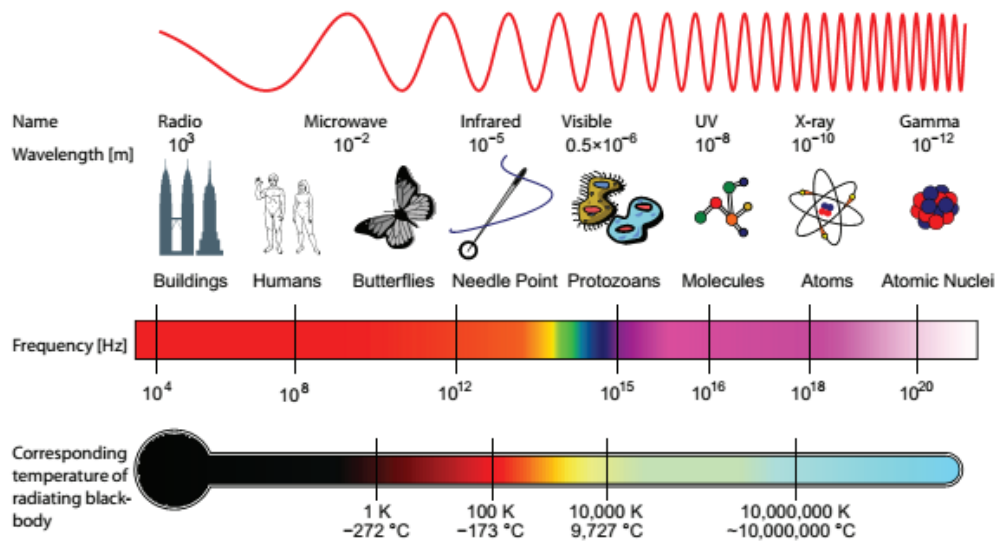


Figure 1.9: Wavelengths and frequencies in the electromagnetic spectrum.

In the SPARC_LAB's line one, see figure 1.10, there are six undulators everyone with: 75 periods, $\lambda_u = 2,8 \text{ cm}$ and can reach a $K_{max} = 2,2$.

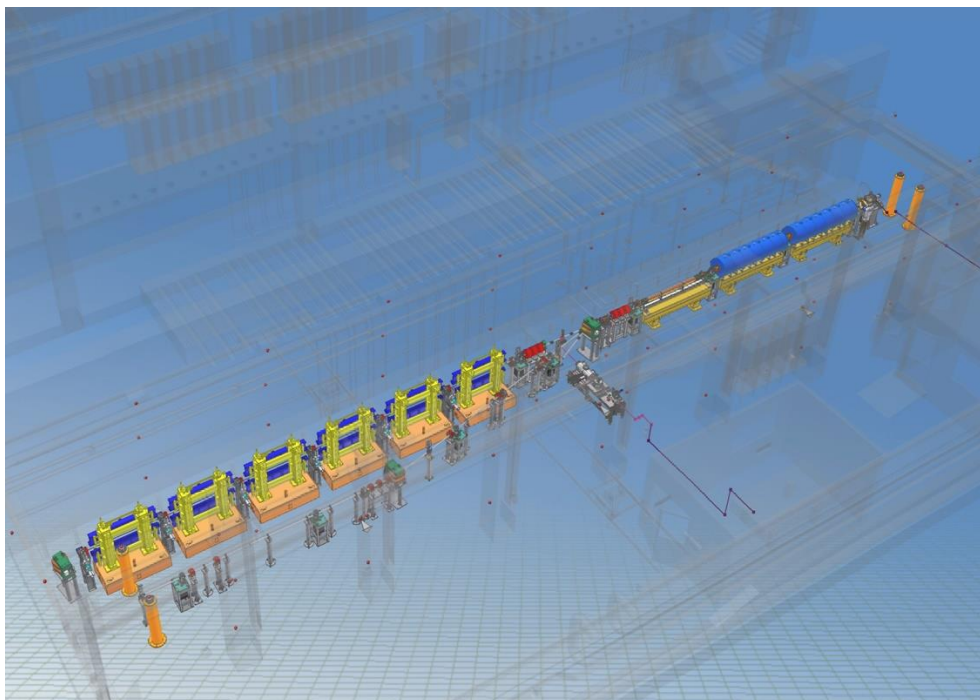


Figure 1.10: Layout of the SPARC_LAB FEL. On the left, in the line one, there are the six undulators.

The SPARC_LAB FEL is able to work in SASE (Self Amplified Spontaneous Emission) and seeding scheme, and with High Harmonic Generation (HHG), with this scheme it has been reached a generation of photons with a wavelength of 40 *nm*.

1.6 Plasma acceleration experiments at SPARC_LAB

With the SPARC photoinjector a new technique called Laser Comb [28], aiming to produce a train of short electron bunches, has been tested [29]. Coherent excitation of plasma waves in plasma accelerators [30] can be also performed with this technique. Preliminary simulations [31] have shown that a train of three electron drive bunches, each of them 25 μm long, with 200 *pC* at 150 *MeV* and 1 μm rms normalized emittance, could accelerate up to 250 *MeV* a 20 *pC*, 10 μm long witness bunch, injected at the same initial energy in a 10 *cm* long plasma of wavelength 383 μm . As shown in Figure 1.11, the drive bunches will lose energy to excite the plasma accelerating field up to 1 *GV/m* in favor of the witness bunch. Simulations show also that the witness bunch can preserve a high quality with a final energy spread less than 1% and 1.6 μm rms normalized emittance. A test experiment named COMB is foreseen at SPARC_LAB, aiming to produce a high quality plasma accelerated beam able to drive a FEL in the SASE mode.

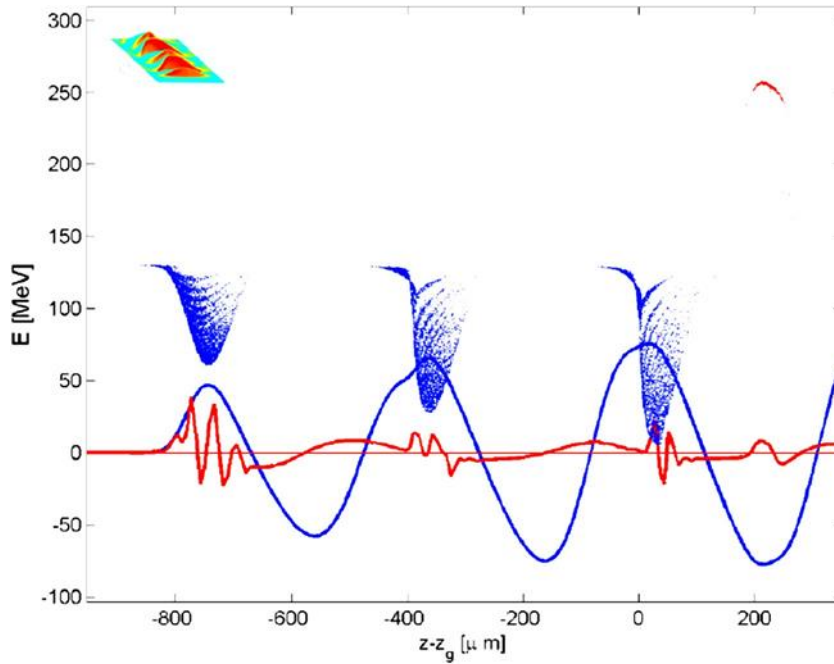


Figure 1.11: . Longitudinal phase space of the COMB beam at the end of the acceleration process. The accelerating field is also plotted in arbitrary units.

In addition to the PWFA experiment, another configuration of plasma acceleration is foreseen at SPARC_LAB. It exploits the LWFA scheme. The compressed laser pulse of FLAME excites a plasma wave, and a bunch produced by SPARC is injected in the trailing area at a proper distance from the laser pulse. The plasma wavelength must be long enough to allow an easy injection, i.e. an accurately chosen time of arrival of the electron bunch. Moreover, since the e-bunches cannot be arbitrarily short, in order to reduce the final energy spread, the accelerating field curvature shall be small on the bunch length scale. This means longer plasma wavelength and, in turn, an average accelerating field, which will be much lower than the one produced in self-injection experiments (up to 1 TV/m) due to the fact that the plasma density will be up to some 10^{17} cm^{-3} , producing a field intensity in the range of few to few tens of GV/m.

To yield a significant increase of the bunch energy, the active accelerating length shall then be in the order of few to few tens of cm , which is much longer than the typical Rayleigh length of a laser pulse. This means a device capable of driving the laser pulse is needed. Our choice is to employ a glass capillary with an internal diameter ranging from about 50 up to 200 or more μm . A leakage of laser energy is foreseen from the capillary inner surface, but it can be shown to be negligible or tolerable for a wide range of inner capillary diameters of practical interest [32].

As a starting working set up we chose a capillary internal diameter of $D_{cap} = 200 \mu m$, which should represent a relaxed target for pointing issues, and a plasma density $n_0 = 10^{17}$; with D_{cap} being large, the expected characteristic decaying length for the laser energy is larger than 7 m . The expected laser energy at the capillary entrance is up to 3.5 J . Preliminary simulations show that it is possible to excite an almost (longitudinally) linear plasma wave with an average accelerating field of about 1.8 GV/m . Assuming a capillary length of 20 cm , the accelerated electron beam possesses fairly good overall properties assuming the injected bunch has the global parameters reported in Table 1.3.

	Plasma entrance	Plasma exit
Charge	5 pC	5 pC
σ_{tr}	10 μm	3.6 μm
σ_z	3.5 μm	3.5 μm
$\Delta\gamma/\gamma$	10^{-3}	$5 \cdot 10^{-2}$
Energy	160 MeV	565 MeV

Table 1.3. LWFA expected parameters.

A test experiment named EXIN (EXternal INjection) is foreseen at SPARC_LAB, and an extensive simulation campaign is ongoing in order to asses other interesting working points, enabling to reach energies in the

order of GeV , while preserving the beam brightness. To this end, a sound procedure to match the bunch from the plasma channel to vacuum, at the capillary end, is in need, preventing the unacceptable normalized emittance dilution foreseen in [33]. Switching to a mild non-linear regime will produce more intense accelerating fields. The trade-off is a larger field curvature and a higher energy spread. In such a set up, an increase of the bunch charge could develop a quite large amount of beam loading that can be used, if the bunch is properly injected, to mitigate the curvature driven energy spread [34].

Chapter 2

Beam dynamics

In this Chapter after an introduction on the particle accelerator, is described the beam dynamics theory with the emittance concept until arriving to the envelope equation for the bunch. At the end of the Chapter there is the description of the production of ultrashort electron bunches with low emittance at SPARC_LAB.

2.1 Particle accelerator

One of the applications of accelerators is particle physics, allowing to answer questions concerning the nature of the universe and its elementary constituents. By accelerating two charged particle beams to nearly the speed of light and colliding them together it is possible to reach center of mass energies of about 10 TeV , giving the possibility to recreating the conditions that existed few instants after the Big Bang. For instance, by analysing the particles produced by the collisions it can be understood how the different types of forces existing in nature are all connected and described by a unified theory. Unfortunately, as one gets closer and closer to solve this kind of questions, particle accelerators of ever greater power (and cost) are needed in order to increase the center of mass energy, as shown in Figure 2.1. Today the most powerful particle accelerator used in particle physics is LHC at CERN, on the French-Swiss border, consisting in a 8.6 km diameter ring where proton-beams of 7 TeV collide to produce, among others, the Higgs boson whose discovery was announced in 2012.

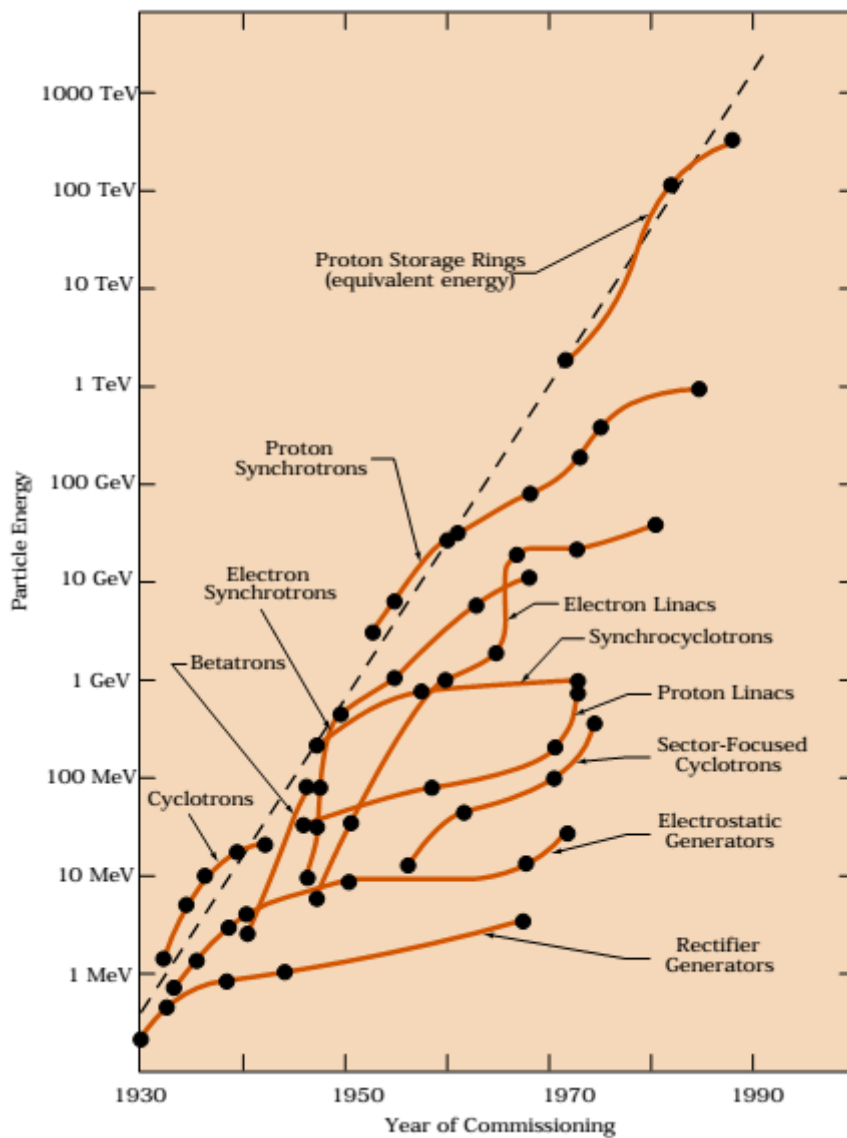


Figure 2.1: Progress in collision energy over time. From [35].

Besides this usage, another application of particle accelerators consists in the generation of advanced radiation sources, a powerful tool in many areas of science, e.g. condensed matter physics, molecular biology, chemistry, material science and medicine. Today the most powerful radiation source, based on the emission of synchrotron radiation, is the Free Electron Laser (FEL). It is able to produce peak brilliance up to $10^{35} s^{-1} m^{-2} rad^{-2}$ (see Figure 2.2) by using the accelerated electrons as gain media for the lasing

process. Both the wide spectrum (from microwaves to X-rays) and the high brilliance offer unique conditions for spectroscopy and X-ray crystallography. Being the radiation emitted in very short pulses, typically less than a picosecond, time resolved measurements can be done, too. Since, as seen in the previous section 1.5, in such a machine the emitted wavelength is $\lambda \propto \gamma^{-2}$, where γ is the Lorentz factor, also in this case high energies are needed in order to reach short wavelengths [36].

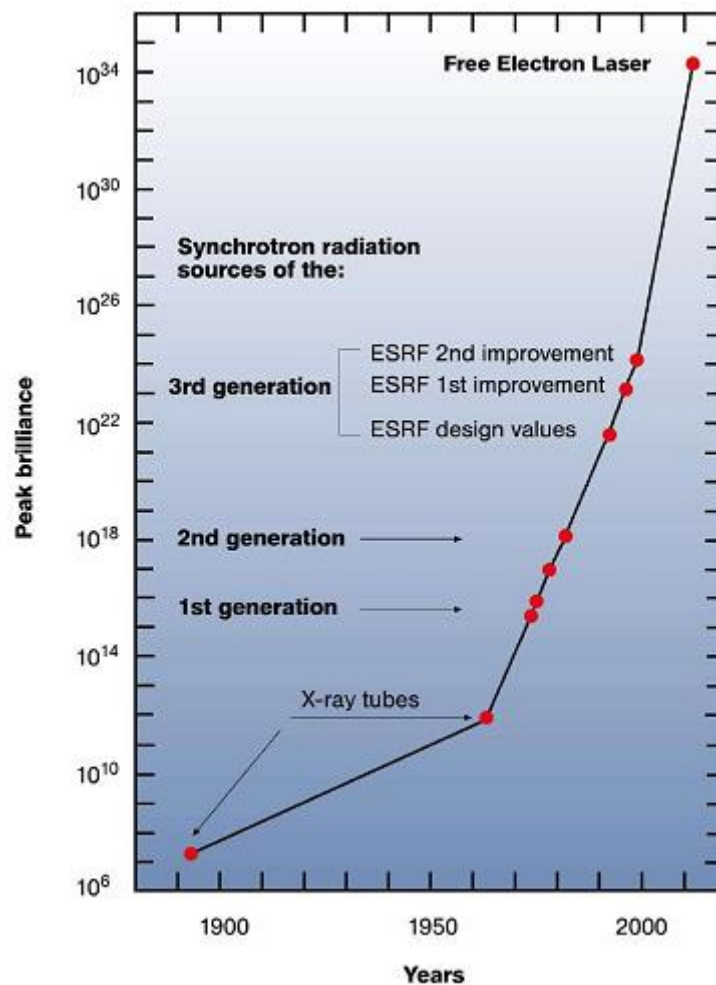


Figure 2.2: History of the peak brilliance of X-ray light sources. Every step corresponds to a new developed technology; in the last section the steepness is very large, indicating a very high brightness produced by Free Electron Laser (FEL). From [37].

2.2 Limits for traditional accelerators

Basically, a conventional machine accelerates particles with an electric field that moves along the accelerator synchronously with the particles. A structure called *slow-wave cavity* (a metallic pipe with periodically placed irises) drives a high power radiofrequency (RF) wave generated by a klystron. The use of a metallic structure limits the accelerating gradient. Depending from the geometry, the material and other technological issues, with fields higher than about 100 MV/m electrical breakdown occurs, sparks jump and current discharges from the walls of the cavities. This limitation makes a TeV linear accelerator quite long, of the order of 30 km, expensive and difficult to build in a short term.

Actual machines can thus accelerate particles by at most a few tens of MeV per meter; the world's longest linear accelerator, the SLC at SLAC, has a maximum gradient of approximately 17 MV/m . Going to higher RF frequencies power sources, peak gradients of about 153 MV/m have been achieved by using coppermolybdenum cavities [38]. There is a variety of proposals to extend conventional micro-wave technology, but all appear limited in the increasing of the gradient to perhaps 150 MV/m , as for the CLIC project [39]. LHC-scale accelerators are very close to the limit of what it is possible to build using conventional technologies (see Figure 2.3). The International Linear Collider (ILC), a proposed 1 TeV lepton collider, is estimated to cost 7 G€ and extend over 30 km in length; at the end, its projected accelerating gradient will be only about twice that of the 40 year old SLC.

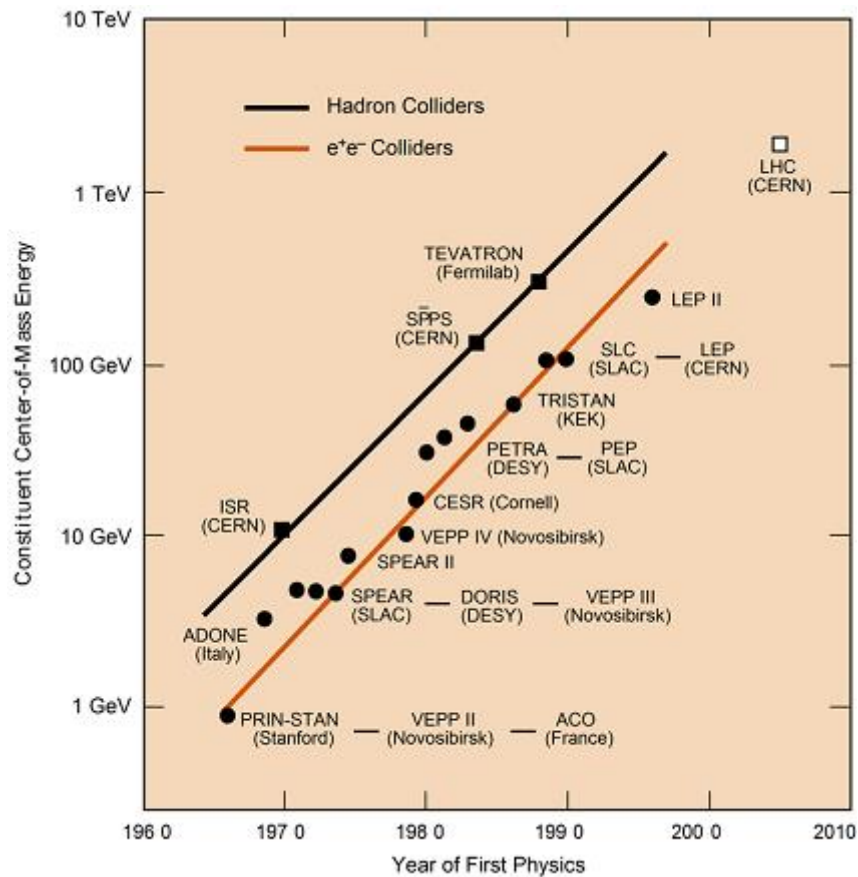


Figure 2.3: Progress in collision energy over time for different facilities. From [35].

The main reason why the costs scaled with the energy is that the accelerating gradients (i.e. the energy gained per unit length) have more or less remained constant over the past few decades, of the order of 10 – 100 MV/m and this is because the fundamental limits derive from the properties of the materials from which they are constructed, because damages occur when the electric fields or the power deposited in a cavity are too intense. The maximum electric field E achievable is limited by a process known as RF breakdown. An expression for the breakdown threshold in metals was obtained empirically from early experimental data gathered in the 1950's:

$$E_s[MV/m] = 220(f[GHz])^{1/3} \quad (2.1)$$

this relation is known as the Kilpatrick Limit. Therefore various materials have been tested during the years in order to find the one with the higher damage threshold [40].

2.3 Basic principles on beam focusing and transport

To preserve the beam quality in the injection in plasma we must achieve matching conditions between these. For this aim introduce the main concepts of beam focusing and transport in modern accelerators using the beam envelope equation as a convenient mathematical tool.

2.3.1 Laminar and non-laminar beams

An ideal high charge particle beam has orbits that flow in layers that never intersect, as occurs in a laminar fluid. Such a beam is often called laminar beam. More precisely a laminar beam satisfies the following two conditions [41]:

1. All particles at a given position have identical transverse velocities. On the contrary the orbits of two particles that start at the same position could separate and later cross each other.
2. Assuming the beam propagates along the z axis, the magnitudes of the slopes of the trajectories in the transverse directions x and y , given by

$x'(z) = dx/dz$ and $y'(z) = dy/dz$, are linearly proportional to the displacement from the axis z of beam propagation.

Trajectories of interest in beam physics are always confined inside of small, near-axis regions, and the transverse momentum is much smaller than the longitudinal momentum, $p_{x,y} \ll p_z \approx p$. As a consequence is convenient in most cases to use the small angle, or paraxial approximation, which allows us to write the useful approximate expressions, $x' = \frac{p_x}{p_z} \approx \frac{p_x}{p}$ and $y' = \frac{p_y}{p_z} \approx \frac{p_y}{p}$.

To help understanding the features and the advantages of a laminar beam propagation, the following figures compare the typical behavior of a laminar and of a non-laminar (or thermal) beam.

Figure 2.4 illustrates an example of orbits evolution of a laminar beam with half width x_0 along a simple beam line with an ideal focusing element (solenoid, magnetic quadrupoles or electrostatic transverse fields are usually adopted to this end), represented by a thin lens located at the longitudinal coordinate $z = 0$. In an ideal lens focusing (defocusing) forces are linearly proportional to the displacement from the symmetry axis z so that the lens maintains the laminar flow of the beam.

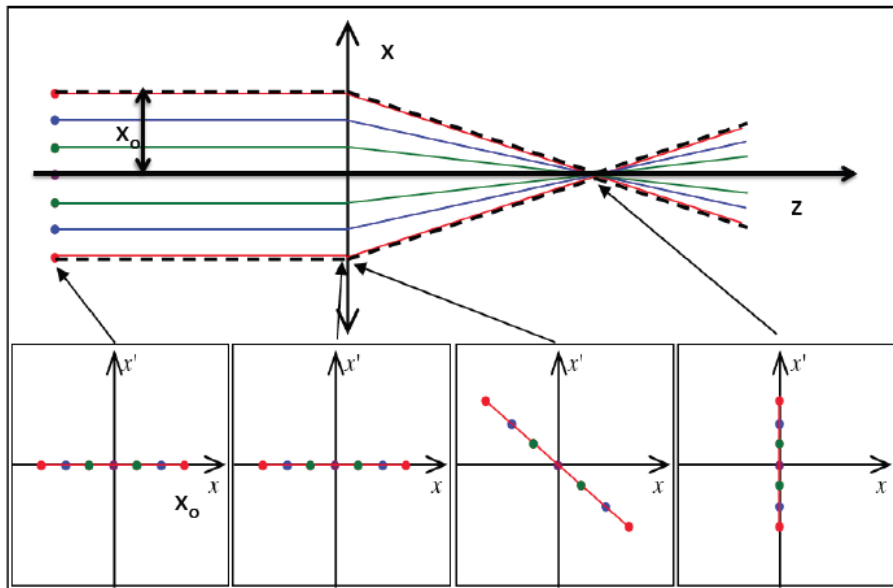


Figure 2.4: Particle trajectories and phase space evolution of a laminar beam

The beam of Figure 2.4 starts propagating completely parallel to the symmetry axis z ; in this particular case particles have all zero transverse velocity. There are no orbits that cross each other in such a beam. Neglecting collisions and inner forces, like Coulomb forces, such a parallel beam could propagate an infinite distance with no change in its transverse width. When the beam crosses the ideal lens it is transformed in a converging laminar beam. Because the transverse velocities after the linear lens are proportional to the displacement off axis, particle orbits define similar triangles that converge to a single point. After passing through the singularity at the focal point, the particles follow diverging orbits. We can always transform a diverging (or converging) beam to a parallel beam by using a lens of the proper focal length, as can be seen reversing the propagation axis of Figure 2.4.

The small boxes in the lower part of figure depict the particle distributions in the trace space (x, x') , equivalent to the canonical phase space $(x, p_x \approx$

$x'p$) when p is constant i.e. without beam acceleration. The phase space area occupied by an ideal laminar beam is a straight line of zero thickness. As can be easily verified the condition that the particle distribution has zero thickness proceeds from condition 1; the line straightness is a consequence of condition 2. The distribution of a laminar beam propagating through a transport system with ideal linear focusing elements is thus a straight line with variable length.

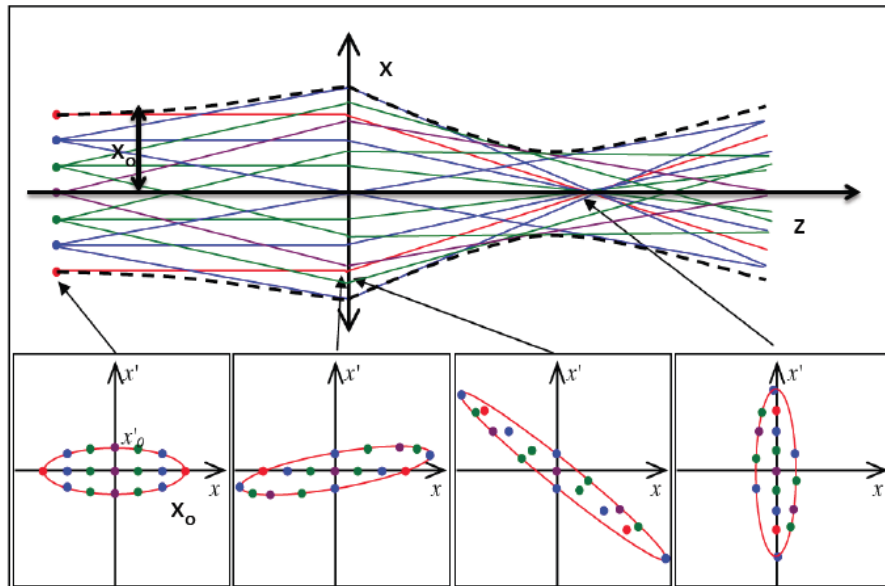


Figure 2.5: Particle trajectories and phase space evolution of a non-laminar beam

Particles in a non-laminar beam have a random distribution of transverse velocities at the same location and a spread in directions, as shown in Figure 2.5. Because of the disorder of a non-laminar beam, it is impossible to focus all particles from a location in the beam toward a common point. Lenses can influence only the average motion of particles. Focal spot limitations are a major concern for a wide variety of applications, from electron microscopy

to free electron lasers and linear colliders. The phase space plot of a non-laminar beam is not anymore a straight line: the beam, as shown in the lower boxes of Figure 2.5, occupies a wider area of the phase space.

2.3.2 The emittance concept

The phase space surface A occupied by a beam is a convenient figure of merit to designate the quality of a beam. This quantity is the emittance ε_x and is represented by an ellipse that contains the whole particle distribution in the phase space (x, x') , such that $A = \pi\varepsilon_x$. An analogous definition holds for the (y, y') and (z, z') planes. The original choice of an elliptical shape comes from the fact that when linear focusing forces are applied to a beam, the trajectory of each particle in phase space lies on an ellipse, which may be called the trajectory ellipse. Being the area of the phase space, the emittance is measured in $[mm - mrad]$ or more often in $[\mu m]$.

The ellipse equation is written as:

$$\gamma_x x^2 + 2\alpha_x x x' + \beta_x x'^2 = \varepsilon_x \quad (2.2)$$

where x and x' are the particle coordinates in the phase space and the coefficients $\alpha_x(z), \beta_x(z), \gamma_x(z)$ are called Twiss parameters which are related by the geometrical condition:

$$\beta_x \gamma_x - \alpha_x^2 = 1 \quad (2.3)$$

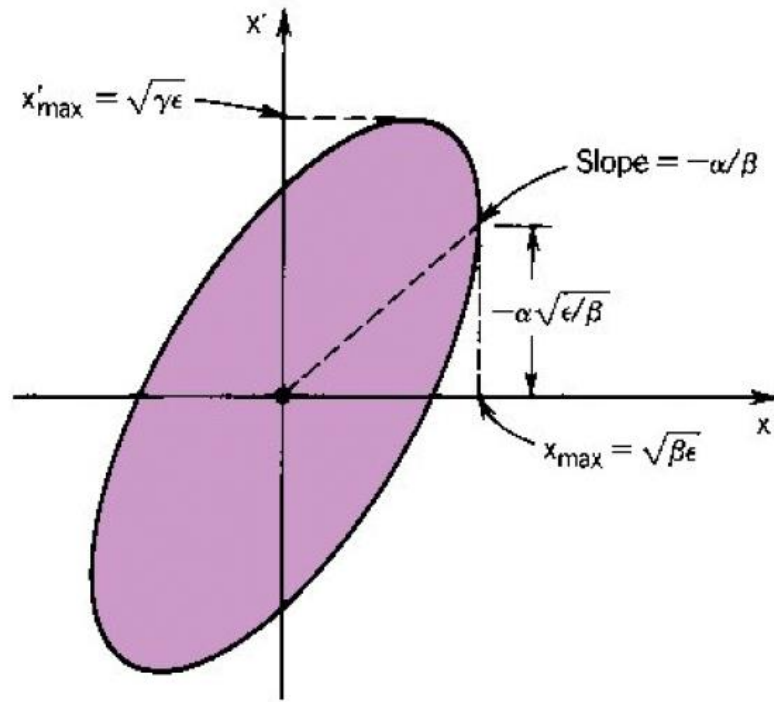


Figure 2.6: Phase space distribution in a skewed elliptical boundary showing relationship of Twiss parameters to the ellipse geometry [41].

As shown in Figure 2.6 the beam envelope boundary X_{max} , its derivative $(X_{max})'$ and the maximum beam divergency (X'_{max}) , i.e. the projection on the axis x and x' of the ellipse edges, can be expressed as a function of the ellipse parameters:

$$\begin{cases} X_{max} = \sqrt{\beta_x \epsilon_x} \\ (X_{max})' = -\alpha \sqrt{\frac{\epsilon}{\beta}} \\ X'_{max} = \sqrt{\gamma_x \epsilon_x} \end{cases} \quad (2.4)$$

According to Liouville theorem the 6D (x, p_x, y, p_y, z, p_z) phase space volume occupied by a beam is constant, provided that there are no dissipative forces, no particles lost or created, and no binary Coulomb collisions between particles. Moreover if the forces in the three orthogonal directions are uncoupled, Liouville theorem holds also for each reduced phase space $(x, p_x), (y, p_y), (z, p_z)$ surfaces and hence also emittance remains constant in each plane [42].

Although the net phase space surface occupied by a beam is constant, nonlinear field components can stretch and distort the particle distribution in the phase space and the beam lose its laminar behaviour. A realistic phase space distribution is often well different by a regular ellipse, as shown in the Figure 2.7.

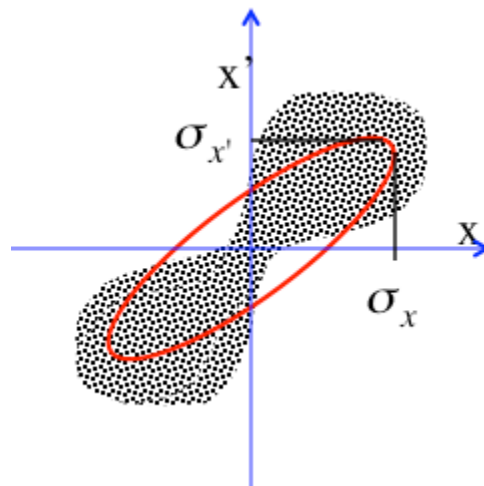


Figure 2.7: Typical evolution of phase space distribution (black dots) under the effects of non linear forces with superimposed the equivalent ellipse (red line).

We introduce, therefore, a definition of emittance that measures the beam quality rather than the phase space area. It is often more convenient to associate to a generic distribution function $f(x, x', z)$ in the phase space a statistical definition of emittance, the so called rms emittance:

$$\gamma_x x^2 + 2\alpha_x x x' + \beta_x x'^2 = \varepsilon_{x,rms} \quad (2.5)$$

such that the ellipse projections on the x and x' axes are equal to the rms values of the distribution, implying the following conditions:

$$\begin{cases} \sigma_x = \sqrt{\beta_x \varepsilon_{x,rms}} \\ \sigma_{x'} = \sqrt{\gamma_x \varepsilon_{x,rms}} \end{cases} \quad (2.6)$$

where:

$$\begin{cases} \sigma_x^2(z) = \langle x^2 \rangle = \int_{-\infty}^{+\infty} \int_{-\infty}^{+\infty} x^2 f(x, x', z) dx dx' \\ \sigma_{x'}^2(z) = \langle x'^2 \rangle = \int_{-\infty}^{+\infty} \int_{-\infty}^{+\infty} x'^2 f(x, x', z) dx dx' \end{cases} \quad (2.7)$$

are the second moments of the distribution function $f(x, x', z)$. Another important quantity that accounts for the degree of (x, x') correlations is defined as:

$$\sigma_{xx'}(z) = \langle xx' \rangle = \int_{-\infty}^{+\infty} \int_{-\infty}^{+\infty} xx' f(x, x', z) dx dx' \quad (2.8)$$

From relations (2.4) it holds also $\sigma_{x'} = \frac{\sigma_{xx'}}{\sigma_x}$, see also 2.15, which allows us to link the correlation moment (2.8) to the Twiss parameter as:

$$\sigma_{xx'} = -\alpha_x \varepsilon_{x,rms} \quad (2.9)$$

One can easily demonstrate using the definitions 2.7 and 2.9 that holds the relation: $\alpha_x = -\frac{1}{2} \frac{d\beta_x}{dz}$.

By substituting the Twiss parameter defined by 2.6 and 2.9 into the condition 2.3 we obtain [43]:

$$\frac{\sigma_{x'}^2}{\varepsilon_{x,rms}} \frac{\sigma_x^2}{\varepsilon_{x,rms}} - \left(\frac{\sigma_{xx'}}{\varepsilon_{x,rms}} \right)^2 = 1 \quad (2.10)$$

Reordering the terms in 2.9 we end up with the definition of rms emittance in terms of the second moments of the distribution:

$$\varepsilon_{rms} = \sqrt{\sigma_x^2 \sigma_{x'}^2 - \sigma_{xx'}^2} = \sqrt{\langle x^2 \rangle \langle x'^2 \rangle - \langle xx' \rangle^2} \quad (2.11)$$

where we omit, from now on, the subscribed x in the emittance notation: $\varepsilon_{rms} = \varepsilon_{x,rms}$. Rms emittance tells us some important information about phase space distributions under the effect of linear or non-linear forces acting on the beam. Consider for example an idealized particle distribution in phase space that lies on some line that passes through the origin as illustrated in Figure 2.8.

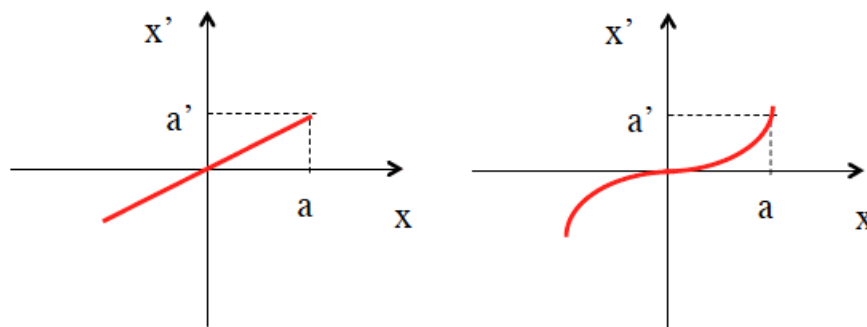


Figure 2.8: Phase space distributions under the effect of linear (left) or non-linear (right) forces acting on the beam

Assuming a generic correlation of the type $x' = Cx^n$ computing the rms emittance according to 2.11 we have:

$$\varepsilon_{rms}^2 = \sqrt{\langle x^2 \rangle \langle x^{2n} \rangle - \langle x^{n+1} \rangle^2} \quad \text{with:} \quad \begin{cases} \varepsilon_{rms} = 0, & n = 1 \\ \varepsilon_{rms} \neq 0, & n > 1 \end{cases} \quad (2.12)$$

When $n = 1$ the line is straight and the rms emittance is $\varepsilon_{rms} = 0$. When $n > 1$ the relationship is nonlinear, the line in phase space is curved, and the rms emittance is in general not zero. Both distributions have zero area.

Therefore, we conclude that even when the phase-space area is zero, if the distribution lies on a curved line its rms emittance is not zero. The rms emittance depends not only on the area occupied by the beam in phase space but also on distortions produced by non-linear forces.

If the beam is subject to acceleration it is more convenient to define what is called the rms normalized emittance, for which the transverse momentum p_x is used instead of the divergence:

$$\varepsilon_{n,rms} = \sqrt{\sigma_x^2 \sigma_{p_x}^2 - \sigma_{xp_x}^2} = \sqrt{\langle x^2 \rangle \langle p_x^2 \rangle - \langle xp_x \rangle^2} \quad (2.13)$$

The reason for introducing a normalized emittance is that the transverse momenta p_x of the particles are unaffected by longitudinal acceleration, while the divergences of the particles are reduced during acceleration because $x' = \frac{p_x}{p}$ when p increases. Thus acceleration reduces the un-normalized emittance but does not affect the normalized emittance. Assuming small energy spread within the beam, the normalized and un-normalized emittances can be related by the approximated relation:

$$\varepsilon_{n,rms} = \langle \beta \gamma \rangle \varepsilon_{rms}$$

2.3.3 The rms envelope equation

We are now interested to follow the evolution of the particle distribution during beam transport and acceleration. One can take profit of the first

collective variable defined in equation 2.7, the second moment of the distribution termed rms beam envelope, to derive a differential equation suitable to describe the rms beam envelope dynamics [44]. To this end lets compute the first and second derivative of σ_x [45], assuming $f'(z) = 0$:

$$\frac{d\sigma_x}{dz} = \frac{d}{dz} \sqrt{\langle x^2 \rangle} = \frac{1}{2\sigma_x} \frac{d}{dz} \langle x^2 \rangle = \frac{1}{2\sigma_x} \frac{d}{dz} 2\langle xx' \rangle = \frac{\sigma_{xx'}}{\sigma_x} \quad (2.14)$$

$$\begin{aligned} \frac{d^2\sigma_x}{dz^2} &= \frac{d}{dz} \frac{\sigma_{xx'}}{\sigma_x} = \frac{1}{\sigma_x} \frac{d\sigma_{xx'}}{dz} - \frac{\sigma_{xx'}^2}{\sigma_x^3} = \frac{1}{\sigma_x} (\langle x'^2 \rangle + \langle xx'' \rangle) - \frac{\sigma_{xx'}^2}{\sigma_x^3} = \\ &= \frac{\sigma_{x'}^2 + \langle xx'' \rangle}{\sigma_x} - \frac{\sigma_{xx'}^2}{\sigma_x^3} \end{aligned} \quad (2.15)$$

Rearranging the second derivative 2.15 we obtain a second order non-linear differential equation for the beam envelope evolution:

$$\sigma_x'' = \frac{\sigma_x^2 \sigma_{x'}^2 - \sigma_{xx'}^2}{\sigma_x^3} + \frac{\langle xx'' \rangle}{\sigma_x} \quad (2.16)$$

or in a more convenient form using the rms emittance definition 2.11:

$$\sigma_x'' - \frac{1}{\sigma_x} \langle xx'' \rangle = \frac{\varepsilon_{rms}}{\sigma_x^3} \quad (2.17)$$

In the equation 2.17 the emittance term can be interpreted physically as an outward pressure on the beam envelope produced by the rms spread in trajectory angle, which is parameterized by the rms emittance.

Lets now consider for example the simple case with $\langle xx'' \rangle = 0$, describing a beam drifting in the free space. The envelope equation reduces to:

$$\sigma_x^3 \sigma_x'' = \varepsilon_{rms}^2 \quad (2.18)$$

With initial conditions σ_0, σ_0' at z_0 , depending on the upstream transport channel, equation (2.18) has a hyperbolic solution:

$$\sigma(z) = \sqrt{(\sigma_0 + \sigma_0'(z - z_0))^2 + \frac{\varepsilon_{rms}}{\sigma_0^2} (z - z_0)^2} \quad (2.19)$$

Considering the case $\sigma_0' = 0$ (beam at waist) and using definition 2.6 the solution 2.19 is often written in terms of the β function as:

$$\sigma(z) = \sigma_0 \sqrt{1 + \left(\frac{z - z_0}{\beta_w}\right)^2} \quad (2.20)$$

This relation indicates that without any external focusing element the beam envelope increases from the beam waist by a factor $\sqrt{2}$ with a characteristic length $\beta_w = \frac{\sigma_0^2}{\varepsilon_{rms}}$ as shown in Figure 2.9.

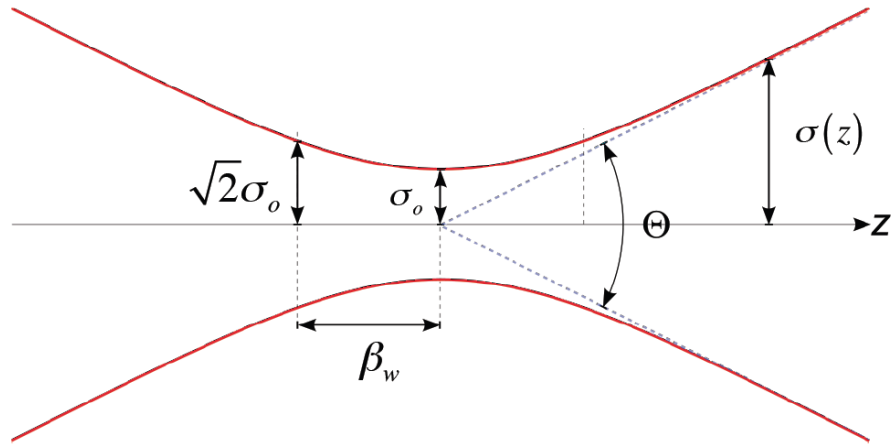


Figure 2.9: Schematic representation of the beam envelope behaviour near the beam waist.

The solution 2.20 is exactly analogous to that of a Gaussian light beam for which the beam width $w = 2\sigma_{ph}$ increases away from its minimum value at the waist w_0 with characteristic length $Z_R = \frac{\pi w_0^2}{\lambda}$ (Rayleigh length) [45]. This analogy suggests that we can identify an effective emittance of a photon beam as $\varepsilon_{ph} = \frac{\lambda}{4\pi}$.

For an effective transport of a beam with finite emittance is mandatory to make use of some external force providing beam confinement in the transport or accelerating line. The term $\langle xx'' \rangle$ accounts for external forces when we know x'' given by the single particle equation of motion:

$$\frac{dp_x}{dt} = F_x \quad (2.21)$$

Under the paraxial approximation $p_x \ll p = \beta\gamma mc$ the transverse momentum p_x can be written as $p_x = px' = \beta\gamma m_0 cx'$, so that:

$$\frac{dp_x}{dt} = \frac{d}{dt}(px') = \beta c \frac{d}{dz}(px')F_x \quad (2.22)$$

and the transverse acceleration results to be

$$x'' = -\frac{p'}{p}x' + \frac{F_x}{\beta cp} \quad (2.23)$$

It follows that:

$$\langle xx'' \rangle = -\frac{p'}{p}\langle xx' \rangle + \frac{\langle xF_x \rangle}{\beta cp} = -\frac{p'}{p}\sigma_{xx'} + \frac{\langle xF_x \rangle}{\beta cp} \quad (2.24)$$

Inserting 2.24 in equation 2.17 and recalling equation 2.15 $\sigma_x' = \frac{\sigma_{xx'}}{\sigma_x}$, the complete rms envelope equation results to be:

$$\sigma_x'' + \frac{p'}{p}\sigma_x' - \frac{1}{\sigma_x} \frac{\langle xF_x \rangle}{\beta cp} = \frac{\varepsilon_{n,rms}^2}{\gamma^2 \sigma_x^3} \quad (2.25)$$

where we have included the normalized emittance $\varepsilon_{rms} = \gamma\varepsilon_{rms}$. Notice that the effect of longitudinal accelerations appears in the rms envelope

equation as an oscillation damping term, called “adiabatic damping”, proportional to $\frac{p'}{p}$. The term $\langle xF_x \rangle$ represents the moment of any external transverse force acting on the beam, as the one produced by a focusing magnetic channel.

2.3.4 External forces

Lets now consider the case of external linear force acting on the beam in the form $F_x = \mp k^2 x$. It can be focusing or defocusing according to the sign. The moment of the force results to be:

$$\langle xF_x \rangle = \mp k^2 \langle x^2 \rangle = \mp k^2 \sigma_x^2 \quad (2.26)$$

and the envelope equation becomes:

$$\sigma_x'' + \frac{\gamma'}{\gamma} \sigma_x' \mp k_{ext}^2 \sigma_x = \frac{\varepsilon_{n,rms}^2}{\gamma^2 \sigma_x^3} \quad (2.27)$$

where we have explicitly used the momentum definition $p = \gamma mc$ for a relativistic particle with $\beta \approx 1$ and defined the normalized focusing strength

$$k_{ext}^2 = \frac{k^2}{\gamma m_0 c^2}.$$

Typical focusing elements are quadrupoles and solenoids [42]. The magnetic quadrupole field in Cartesian coordinates is given by:

$$\begin{cases} B_x = B_0 \frac{y}{d} = B'_0 y \\ B_y = B_0 \frac{x}{d} = B'_0 x \end{cases} \quad (2.28)$$

where d is the pole distance and B'_0 the field gradient. The force acting on the beam is $\vec{F}_\perp = qv_z B'_0 (y\hat{j} - x\hat{i})$ that, when B_0 is positive, is focusing in the x direction and defocusing in y . Using two quadrupoles is it possible to focus the beam in both direction x and y . Using a triplet of quadrupoles is it possible to focus in both direction x, y and is also possible to reach cylindrical symmetry [41]. The focusing strength in a quadrupole is $k_{quad}^2 = \frac{qB'_0}{\gamma m_0 c}$.

In a solenoid the focusing strength is given by: $k_{sol}^2 = \left(\frac{qB_0}{2\gamma m_0 c}\right)^2$. Notice that the solenoid is always focusing in both directions, an important properties when the cylindrical symmetry of the beam must be preserved. On the other hand being a second order quantity in γ it is more effective at low energy.

It is interesting to consider the case of a uniform focusing channel without acceleration described by the rms envelope equation:

$$\sigma_x'' + k_{ext}^2 \sigma_x = \frac{\varepsilon_{rms}^2}{\sigma_x^3} \quad (2.29)$$

By substituting $\sigma_x = \sqrt{\beta_x \varepsilon_{rms}}$ in 2.29 one obtains an equation for the “betatron function” $\beta_x(z)$ that is independent on the emittance term:

$$\beta_x'' + 2k_{ext}^2 \beta_x = \frac{2}{\beta_x} + \frac{\beta_x'^2}{2\beta_x} \quad (2.30)$$

Equation 2.30 containing only the transport channel focusing strength and being independent on the beam parameters, suggests that the meaning of the betatron function is to describe the transport line characteristic by itself. The betatron function reflects exterior forces from focusing magnets and is highly dependent on the particular arrangement of quadrupole magnets. The equilibrium, or matched, solution of equation 2.30 is given by $\beta_{eq} = \frac{1}{k_{ext}} = \frac{\lambda_\beta}{2\pi}$ as one can easily verify. This result shows that the matched β_x function is simply the inverse of the focusing wave number, or equivalently is proportional to the “betatron wavelength” λ_β .

2.3.5 Space charge forces

Another important force acting on the beam is the one produced by the beam itself due to the internal Coulomb forces. The net effect of the Coulomb interaction in a multi-particle system can be classified into two regimes [42]:

- *Collisional regime*, dominated by binary collisions caused by close particle encounters

- *Collective regime* or *space charge regime*, dominated by the self-field produced by the particle's distribution that varies appreciably only over large distances compare to the average separation of the particles.

A measure for the relative importance of collisional versus collective effects in a beam with particle density n is the relativistic *Debye length*:

$$\lambda_D = \sqrt{\frac{\epsilon_0 \gamma^2 k_B T_b}{e^2 n}} \quad (2.31)$$

where the transverse beam temperature T_b is defined as $k_B T_b = \gamma m_0 \langle v_{\perp}^2 \rangle$, and k_B is the Boltzmann constant. As long as the Debye length remains small compared to the particle bunch transverse size the beam is in the space charge dominated regime and is not sensitive to binary collisions. Smooth functions for the charge and field distributions can be used in this case and the space charge force can be treated like an external applied force. The space-charge field can be separated into linear and nonlinear terms as a function of displacement from the beam axis. The linear space-charge term defocuses the beam and leads to an increase in beam size. The nonlinear space-charge terms increase also the rms emittance by distorting the phase-space distribution. Under the paraxial approximation of particle motion we can consider the linear component only. We shall see in the next paragraph that also the linear component of the space charge field can induce emittance growth when correlation along the bunch are taken in to account.

For a bunched beam of uniform charge distribution in a cylinder of radius R and length L , carrying a current \hat{I} and moving with longitudinal velocity $v_z =$

βc , the linear component of the longitudinal and transverse space charge field are approximately given by [46]:

$$\begin{cases} E_z(\zeta) = \frac{\hat{I}L}{2\pi\epsilon_0 R^2 \beta c} h(\zeta) \\ E_r(r, \zeta) = \frac{\hat{I}r}{2\pi\epsilon_0 R^2 \beta c} h(\zeta) \end{cases} \quad (2.32)$$

The field form factor is described by the functions:

$$h(\zeta) = \left[\sqrt{A + (1 - \zeta)^2} - \sqrt{A + \zeta^2} + (2\zeta - 1) \right] \quad (2.33)$$

$$g(\zeta) = \frac{1 - \zeta}{2\sqrt{A^2 + (1 - \zeta)^2}} + \frac{\zeta}{2\sqrt{A^2 + \zeta^2}} \quad (2.34)$$

where $\zeta = \frac{z}{L}$ is the normalized longitudinal coordinate along the bunch and $A = \frac{R}{\gamma L}$ is the beam aspect ratio. The field form factors account for the longitudinal variation of the fields along the bunch. As γ increases $g(\zeta) \rightarrow 1$ and $h(\zeta) \rightarrow 0$ thus showing that space charge fields mainly affect transverse beam dynamics. It shows also that an energy increase corresponds to a bunch lengthening in the moving frame $L' = \gamma L$ leading to a vanishing longitudinal field component, as in the case of a continuous beam in the laboratory frame.

To evaluate the force acting on the beam one must account also for the azimuthal magnetic field associated with the beam current, that in

cylindrical symmetry is given by $B_\theta = \frac{\beta}{c} E_r$. Thus the Lorentz force acting on each single particle is given by:

$$F_r = e(E_r - \beta c B_\theta) = e(1 - \beta^2)E_r = \frac{eE_r}{\gamma^2} \quad (2.35)$$

The attractive magnetic force, which becomes significant at high velocities, tends to compensate for the repulsive electric force. Therefore space charge defocusing is primarily a non-relativistic effect and decreases as γ^{-2} .

In order to include space charge forces in the envelope equation lets start writing the space charge forces produced by the previous fields in Cartesian coordinates:

$$F_x = \frac{eIx}{2\pi\gamma^2\varepsilon_0\sigma_x^2\beta c} g(\zeta) \quad (2.36)$$

Then computing the moment of the force we need:

$$x'' = \frac{F_x}{\beta c p} = \frac{eIx}{2\pi\varepsilon_0\gamma^3 m_0 \sigma_x^2 \beta^3 c^3} g(\zeta) = \frac{k_{sc}(\zeta)}{(\beta\gamma)^3 \sigma_x^2} x \quad (2.37)$$

where we have introduced the generalized beam perveance

$$k_{sc}(\zeta) = \frac{2\hat{I}}{I_A} g(\zeta) \quad (2.38)$$

normalized to the Alfven current $I_A = \frac{4\pi\epsilon_0 m_0 c^3}{e} = 17 \text{ kA}$. Notice that in this case the perveance 2.38 explicitly depends on the slice coordinate ζ . Now we can calculate the term that enters in the envelope equation for a relativistic beam:

$$\langle xx'' \rangle = \frac{k_{sc}}{\gamma^3 \sigma_x^3} \quad (2.39)$$

leading to the complete envelope equation:

$$\sigma_x'' + \frac{\gamma'}{\gamma} \sigma_x' + k_{ext}^2 \sigma_x = \frac{\epsilon_{n,rms}^2}{\gamma^2 \sigma_x^3} + \frac{k_{sc}}{\gamma^3 \sigma_x} \quad (2.40)$$

From the envelope equation 2.40 we can identify two regimes of beam propagation: *space charge dominated* and *emittance dominated*. A beam is space charge dominated as long as the space charge collective forces are largely dominant over the emittance pressure. In this regime the linear component of the space charge force produces a quasi-laminar propagation of the beam as one can see by integrating one time equation 2.37 under the paraxial ray approximation $x' \ll 1$. A measure of the relative importance of space charge effects versus emittance pressure is given by the *laminarity*

parameter, defined as the ratio between the space charge term and the emittance term:

$$\rho = \frac{\hat{I} \sigma^2}{2I_A \gamma \varepsilon_n^2} \quad (2.41)$$

When ρ greatly exceeds unity, the beam behaves like a laminar flow (all beam particles move on trajectories that do not cross) and transport and acceleration require a careful tuning of focusing and accelerating elements in order to keep laminarity. Correlated emittance growth is typical in this regime which can be conveniently made reversible if proper beam matching conditions are fulfilled. When $\rho < 1$ the beam is emittance dominated (thermal regime) and the space charge effects can be neglected. The transition to thermal regime occurs when $\rho \approx 1$ corresponding to the transition energy

$$\gamma_{tr} = \frac{\hat{I} \sigma^2}{2I_A \varepsilon_n^2} \quad (2.42)$$

Take as an example the beam that will be injected in to the plasma during the COMB experiment in which $\hat{I} = 581.4 \text{ A}$, $\varepsilon_n = 0.66 \text{ } \mu\text{m}$ and $\sigma = 8.2 \text{ } \mu\text{m}$ and it will enter in the plasma capillary with an energy of 126.2 MeV . The laminarity parameter for this bunch is $\rho = 0.01$ and it is leaving the space charge dominated regime and is entering the thermal regime at the transition energy of 0.82 MeV . From this example one may conclude that space charge dominated regime is typical of low energy beams. Actually for

applications like linac driven Free Electron Lasers peak current exceeding kA are required. Space charge effects may recur if bunch compressors are active at higher energies and a new energy threshold with higher \hat{I} has to be considered.

2.4 Production of ultrashort electron bunches with low emittance

The production of ultrashort electron bunch, as the one required for plasma acceleration experiments (see Chapter 3), is a subject of investigation that has attracted increasing attention in recent years, spurred by a large number of applications, spanning short wavelength free electron lasers (FEL), THz radiation production, linear colliders and plasma wake field accelerators. Space charge effects at low energy prevent the generation of short electron bunches ($< 1 ps$) with a significant amount of charge ($> 10 pC$) directly from the electron source, leading to emittance degradation and bunch elongation within a few centimeters downstream the cathode. As such, bunch compression is always necessary to shorten the electron pulse to the required length thus achieving a high peak current. The most popular and effective device used thus far is the magnetic compressor in which a bunch with a time-energy correlation (or chirp) is driven along an energy-dependent path length by a dispersive, nonisochronous beam transport section, consisting, in its simplest form, of four dipoles placed in a chicane configuration. The process of magnetic compression may often unacceptably degrade the beam quality, however, due to significant emittance growth caused by coherent synchrotron radiation effects in bends [47].

Another new method termed *velocity bunching*, able to compress the bunch using rectilinear trajectories at relatively low energy [48], which must thus be integrated into the emittance compensation process [49], has been proposed in [50] and tested at SPARC_LAB [51]. The longitudinal phase space rotation in the velocity bunching process is based on a correlated time-velocity chirp in the electron bunch, in such a way that electrons on the tail of the bunch are faster than electrons in the bunch head. This rotation occurs inside the longitudinal potential of a traveling rf wave (longitudinal focusing) which accelerates the beam inside a long multicell rf structure and simultaneously applies an off crest energy chirp to the injected beam. This is possible if the injected beam is slightly slower than the phase velocity of the rf wave so that when injected at the zero crossing field phase it slips back to phases where the field is accelerating, but is simultaneously chirped and compressed. The key point is that compression and acceleration take place at the same time within the same accelerator section, the initial one following the gun.

In order to prevent irreversible emittance growth during bunch compression the key issue is to preserve the laminarity of the beam with an envelope propagated as close as possible to a Brillouin-like flow, represented by an invariant envelope [52] as generalized to the context of beam compression and thus increasing the current I during acceleration. For these kind of beams, mismatches between the space charge correlated forces and the external focusing gradient produce slice envelope oscillations that cause normalized emittance oscillations. It has been shown that to keep such oscillations under control during the velocity bunching, the beam has to be injected into the rf structure with a laminar envelope waist ($\sigma' = \alpha = 0$ see paragraph 2.3.3) and the envelope has to be matched to the accelerating and focusing gradients in such a way to stay close to an

equilibrium mode [52,53]. Ponderomotive rf focusing force are actually too weak in a travelling wave structure [54] to provide sufficient beam focusing. A long solenoid around the accelerating structure is a convenient replacement to provide the necessary focusing. In this configuration the matching condition for the transverse rms envelope is given by:

$$\sigma = \frac{1}{k} \sqrt{\frac{I_0}{4\gamma_0 I_A} \left(1 + \sqrt{1 + \left(\frac{4\varepsilon_n \gamma_0 k I_A}{I_0} \right)^2} \right)} \quad (2.43)$$

where $k = \frac{eB_{sol}}{mc}$, B_{sol} is the solenoid field, $I_A = 17kA$ is the Alfvén current, ε_n the normalized emittance, γ_0 and I_0 are the values for the energy and the current, respectively, at injection into the compressor.

With the SPARC photoinjector a new technique called Laser Comb [55], aiming to produce a train of short electron bunches, has been tested [56]. This technique is relevant for the work discussed in this thesis and deserves a more detailed discussion. In this operating mode, the photocathode is illuminated by a comb-like laser pulse to extract a train of electron bunches injected into the same RF bucket of the gun. The SPARC _LAB laser system, based on a Ti:Sa oscillator has been upgraded for this specific application. The technique used relies on a α -cut beta barium borate (α -BBO) birefringent crystal, where the input pulse is decomposed in two orthogonally polarized pulses with a time separation proportional to the crystal length. In the first accelerating structure operating in the VB mode, i.e., injecting the bunch train near the zero crossing of the RF wave, the bunch train is compressed by the longitudinal focusing effect of the RF wave. Moreover, with a proper choice of injection phase it becomes possible to keep under control both intra-bunch distance and single bunch

length. This method preserves all extracted charge and it is different from other passive techniques [57], where the train is produced by using a mask that stops a significant fraction of the charge. Up to four electron beam pulses shorter than 300 fs and separated by less than 1 ps have been characterized and a narrowing THz spectrum produced by the bunch train has been measured [58]. In addition two electron beam pulses have been injected in the undulator and a characteristic interference spectrum produced by the FEL interaction in this new configuration has been observed. That confirms that both pulses have been correctly matched to the undulator and was both lasing [59].

Chapter 3

Plasma Acceleration

In the next paragraphs will be analyzed the plasma acceleration, in Laser and Plasma wakefield configurations, the focus there will be on the Plasma wakefield acceleration in the quasi non-linear regime.

By accelerating particles more than allowed by the electrical breakdown limit, the accelerator could be made more compact. In a plasma accelerator, the role of the accelerating structure is played by the plasma, a ionized gas, and the power source is not microwave radiation but is either a laser beam or a charged particle beam. The basic idea of a plasma wakefield accelerator is relatively straightforward and seems to have been first proposed by Fainberg in 1956 [60]. He suggested that if plasma waves ($v_{ph} \approx c$) are generated, particles could be accelerated by sampling the relativistic electric fields inside the plasma. At first sight, lasers and charged particle beams do not seem well suited for particle acceleration. They have very strong electric fields, but the fields are mostly perpendicular (transverse) to the direction of propagation. To be effective, the electric field in an accelerator has to point in the direction of the travelling particle, so a longitudinal field is needed. Fortunately, when a laser or charged particle beam is sent through a plasma, interaction with the plasma can create such electric field (see Figure 3.1).

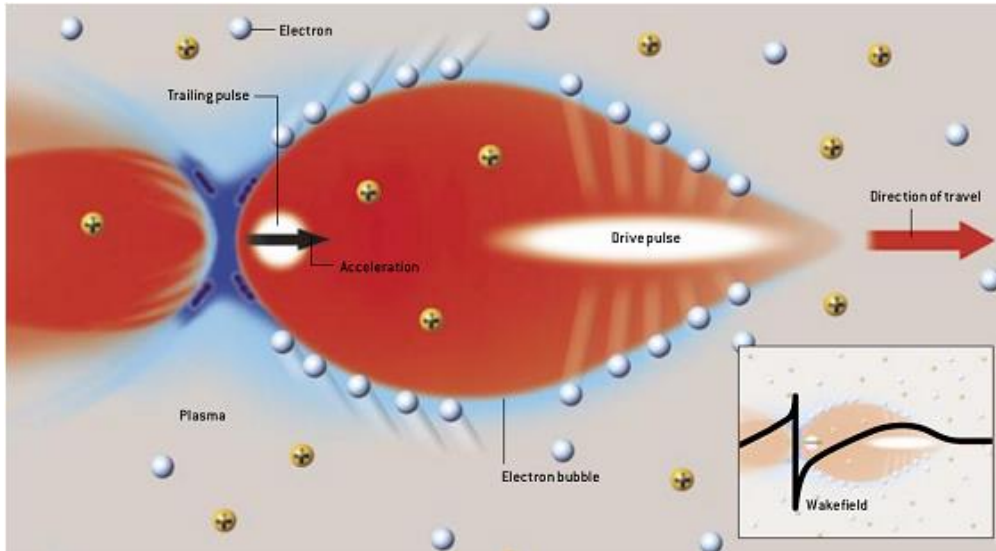


Figure 3.1: Wakefield accelerator relies on a charge disturbance known as *wakefield* to provide the driving force. The drive pulse, which can be a short pulse of either a laser or an electron beam, blows the electrons (blue) in an ionized gas, or plasma, outward leaving behind a region of positive charge (red). The positive charge pulls the negatively charged electrons back in behind the drive pulse, forming an electron bubble around the positive region. Along the axis that the beam propagates, the electric field (plotted below) resembles a very steep ocean wave about to break. The field causes a trailing pulse of electrons caught near the rear of the bubble to feel a very strong forward acceleration. From [61].

The process works in this way: a plasma as a whole is electrically neutral, containing equal amounts of negative charge (electrons) and positive charge (ions). A pulse from an intense laser or particle beam creates a disturbance in the plasma. In essence, the beam pushes the lighter electrons away from the heavier positive ions (that can be assumed fixed) creating two regions of positive and negative charge excesses (see Figure 3.1). The disturbance forms a wave that travels through the plasma at about the speed of light. As a consequence, a powerful electric field points from the

positive to the negative region and accelerates any charged particles that come under its influence.

3.1 Principles of Plasma Acceleration

A plasma medium can support accelerating electric fields \mathbf{E} of very high magnitude [62]. A simple estimate for the strength of the electric field oscillation amplitude can be made starting from Gauss law:

$$\nabla \cdot \mathbf{E} = \frac{\rho}{\epsilon_0} = \frac{e(n_i - n_e)}{\epsilon_0} \quad (3.1)$$

where e is the electron charge, ρ is the charge density, n_i and n_e are, respectively, the ions and electrons densities. The largest wakes occur when all the electrons are “blown out”, so $n_e = 0$ and $n_i = n_0$, where n_0 is the plasma density. Assuming a one-dimensional plane wave perturbation of the charge density, it is $\nabla = \hat{z}\partial/\partial z$ and $n_0(z) = n_0 \exp(ik_p z)$, with wave-number $k_p = \frac{\omega_p}{c}$ (where c is the speed of light in vacuum) and

$$\omega_p = \sqrt{\frac{e^2 n_0}{\epsilon_0 m_e}} \quad (3.2)$$

is the plasma frequency, where e and m_e are the electron charge and rest mass and ϵ_0 is the vacuum dielectric constant. As a first approximation the

plasma electrons can be assumed non-relativistic, thus the electron mass is exactly its rest mass m_e . As a consequence, the electric field perturbation is $E = E_0 \exp(ik_p z)$ and equation 3.1 can be rewritten as:

$$|\nabla \cdot \mathbf{E}| = |-ik_p E_0| = \frac{\omega_p}{c} E_0 = \frac{e}{\epsilon_0} n_0 \quad (3.3)$$

so the electric field amplitude is equal to:

$$E_0 \left[\frac{V}{m} \right] = \frac{m_e c}{e} \omega_p = c \sqrt{\frac{m_e}{\epsilon_0} n_0} \cong 96 \sqrt{n_0 \text{ (cm}^{-3}\text{)}} \quad (3.4)$$

where it is assumed that the ions are fixed in the plasma, due to their much lower plasma frequency¹. The result in equation 3.4 is sometimes referred to as the *cold wave-breaking field* because it is the amplitude at which a cold² plasma wave breaks; it is the equivalent of the Kilpatrick Limit in the RF cavities.

This field can be quite large. Assuming a plasma with 10^{18} cm^{-3} density, a wave with maximum electric field peaks in the order of 100 GV/m (or, equivalently, 1 GV/cm) can be generated, being three order of magnitude

1) The nucleon mass (proton or neutron) is $m_p \approx 2000 m_e$, therefore a nucleus containing A nucleons has a plasma frequency $\sqrt{2000 \cdot A}$ times lower than an electron.

2) A plasma is sometimes referred to as being "hot" if it is nearly fully ionized, i.e. $k_B T > E_i$, where E_i is the gas ionization energy. It is "cold" if only a small fraction (e.g. 1%) of the gas is ionized. In a "cold" plasma, the temperature is typically several thousand degrees Celsius.

more intense than the accelerating gradient in a conventional accelerator powered by microwaves. The physical reason why plasmas can support those high gradients is the collective effect of the plasma electrons. As opposed to the other three states of matter where the particles and molecules are distributed in a disordered and incoherent way, inside a plasma the freed electrons can be manipulated together and forced to act coherently. The drawback is that the wavelength of a plasma wave is $\lambda_p = 2\pi c/\omega_p$, or $\lambda_p(\mu m) \cong 3.3 \times 10^{10}(n_0(cm^{-3}))^{-1/2}$, that is only $33 \mu m$ for $n_0 = 10^{18} cm^{-3}$, whereas the typical RF microwave wavelength is about 10 cm: it is very tricky to place a bunch of electrons in such a microscopic wave. Moreover the accelerating cavity is no longer a static object such as a machined piece of metal or a lithographically produced dielectric surface, but rather something that must be created dynamically each time a particle bunch has to be accelerated.

John M. Dawson first proposed this general method of using plasmas to accelerate particles in 1979 [63]; it took more than a decade before experiments demonstrated electrons surfing plasma waves and gaining energy [64, 65, 66]. Today all the different plasma acceleration schemes can be classified in two main categories, the laser and particle beam driven layouts: in the first case a laser pulse is required to form an electron plasma wave, while in the second one the electron plasma wave is formed by an electron bunch.

3.2 Laser Driven Plasma Accelerators

The paper of Tajima and Dawson [63] proposed a laser-based scheme which are now called Laser Wakefield Acceleration (LWFA), in which a short, high power laser pulse is introduced into the plasma to form an electron plasma wave.

The invention of the chirped-pulse amplifier (CPA, see [67]) enabled the use of a high-power lasers with a pulse width approximately equal to the wavelength of a high-density plasma wave [68, 69], paving the way to the LWFA. The so-called T3 (Table-Top Terawatt) lasers are now commercially available and enabled even small laboratories to perform LWFA experiments.

In this scheme an ultra-short laser pulse is needed; if the longitudinal size of the pulse is about a half (or less) of the plasma wavelength λ_p , a high amplitude plasma wave develops quasi-resonantly on the wake of the pulse, excited by the action of the ponderomotive force of the laser [70] that is:

$$\mathbf{F}_p = -\frac{m_e c^2}{2} \nabla \mathbf{a}^2 = -\frac{e^2}{4m_e \omega_L^2} \nabla E^2 \quad (3.5)$$

where \mathbf{E} is the electric field of the laser, ω_L is the laser frequency and $\mathbf{a} = \frac{e\lambda E}{2\pi m_e c^2}$ is the laser strength parameter.

Focusing a high intensity laser in a gas, the pulse immediately strips off the electrons in the gas, producing a plasma [71] (Figure 3.2(a)). The ponderomotive force of the laser bullet is high enough so that the much lighter electrons are blown outward in all directions, leaving behind the

more massive ions. When they reach the laser pulse propagation axis, they overshoot it and end up travelling outward again, producing a wavelike oscillation (Figure 3.2(b)). The electrons actually form a bubble-like structure, in the front of which there is the laser pulse that creates the plasma. Inside the bubble there are only plasma ions (Figure 3.2(c)). The bubble can be microscopic, of the order of 30 μm in diameter, depending on λ_p . At this point electrons are injected in the trailing area of the bubble and experience an electric field pulling them toward the positive charges inside the bubble (Figure 3.2(d)). If the electrons are injected by an external electron gun the process is called *external-injection*, while if the plasma is in the non-linear regime the plasma itself can self-inject the electrons and the process is called *self-injection*.

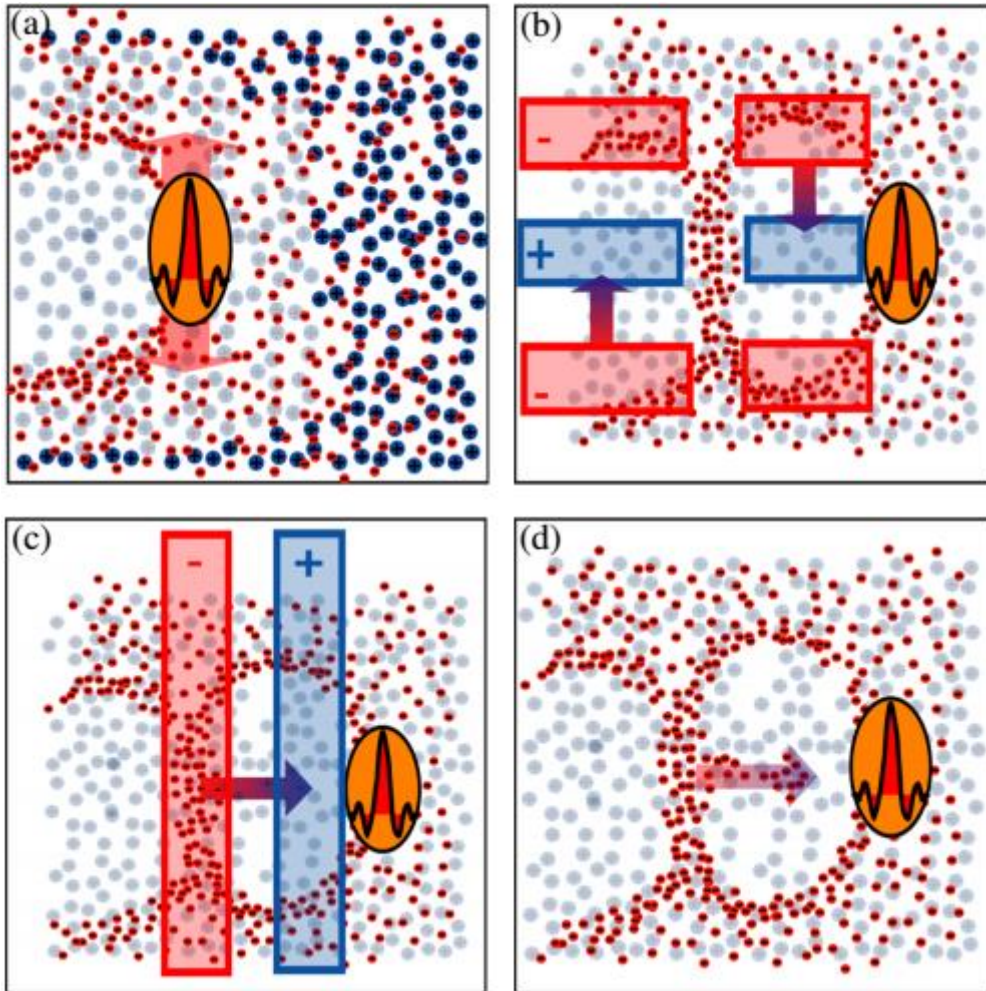


Figure 3.2: Laser Wakefield Acceleration (LWFA). (a) Laser in a gas. A very short laser pulse is focused into a gas; its atoms are ionized in the field of the laser and electrons are expelled from the laser path. (b) Electrons start to oscillate; because the positively charged ions are too heavy to follow the electrons, they remain in place and pull back the expelled electrons. If the laser pulse is shorter than the duration of this plasma oscillation a fully blown out bubble without electrons is created behind the laser. (c) If the conditions for the creation of this bubble regime are satisfied, strong fields in laser direction occur. This wake structure follows the laser pulse as it travels through the plasma and the acceleration field in laser direction occurs. (d) Electrons can get trapped in these accelerating fields and accelerated (GV/m), following the laser pulse. From [72].

In LWFA the plasma essentially receives a single kick from the short laser pulse, therefore the total amount of energy required for a full stage of the accelerator must be contained in a single pulse shorter than a plasma period. For LWFA in the nonlinear regime ($a \gg 1$) the maximum wakefield amplitude is [73]

$$\frac{E_{max}}{E_0} = \frac{a^2}{\sqrt{1 + a^2}} \quad (3.6)$$

where E_0 is the cold nonrelativistic wave breaking field (see equation 3.4).

As an example, a nowadays available laser with power of 100 TW (5.5 J with a pulse duration of 55 fs) operating at 800 nm and focused to a spot size of 18 μm gives a vector potential $a = 3$ and an intensity $I = 1.9 \times 10^{19} \text{ W/cm}^2$. With $n_0 = 10^{18} \text{ cm}^{-3}$, the resulting accelerating gradient is about 150 GV/m.

A drawback of laser accelerators is their short acceleration length l limited by diffraction length. Acceleration is possible only around the focal point of the laser: increasing the laser spot results in a lengthener of the accelerator size and in a weak acceleration gradient.

Another issue is represented by the phase slippage, due to the laser group velocity in a plasma given by $v_g = c[1 - (\lambda_L/\lambda_p)^2]^{1/2}$ (where λ_L is the laser wavelength), which is smaller than the velocity of accelerated electrons (moving at $v_b \approx c$). Due to the slippage, the electrons eventually reaches a decelerating region in the wave; this process is called *dephasing* and limits

the acceleration distance to the dephasing length, that is the distance in which accelerated electrons outstrip the laser wakefield, given by:

$$L_{deph} = \frac{1}{2} \frac{\lambda_p^3}{\lambda_L^2} \times \begin{cases} 1 & \text{if } a \ll 1 \\ (\sqrt{2}/\pi)a/N_p & \text{if } a \gg 1 \end{cases} \quad (3.7)$$

where N_p is the number of plasma periods behind the drive laser pulse.

3.3 Beam Driven Plasma Accelerators

Several years after Tajima and Dawson's review, Chen proposed a scheme which uses particle beams instead of lasers in order to excite plasma waves [66]. The scheme, called Plasma Wakefield Acceleration (PWFA), has not attained so far a larger acceleration gradients than those by laser methods. The working principle relies on a relativistic charged particle bunch moving through a plasma that excites a wakefield in a manner similar to that of an intense laser pulse. It was the PWFA that first produced high charge accelerated particle beams of about 2 nC [74]. Beam-driven and laser-driven methods have much physics in common. While for a laser driver the ponderomotive force expels plasma electrons and initiates a plasma wave, for a relativistic electron bunch the space charge force of the bunch is able to displace the plasma electrons and initiates a wake.

As in the laser-driven schemes, in the PWFA it is possible to consider a self-injection scheme, where an injected electron beam creates the plasma wave and the accelerated electrons are captured from the plasma itself, or an external injection in which one or multiple injected bunches, the *drivers*,

creates the plasma wave that accelerates another injected bunch, the *witness*. As will be discussed in paragraph 3.3.2 the second scheme, in which one or several driver bunches are used in order to enhance the wakefield, is the actually most promising (see Figure 3.13), and will be use in the COMB experiment. First of all, being a PWFA technique it is not limited by diffraction because the bunch travels at a relativistic velocity, i.e. it results "frozen" due to the damping of space-charge forces (see paragraph 2.3.5). Furthermore, it is not limited by dephasing because all the bunches (and the generated plasma wave) travel at the same velocity $v_b \approx c$.

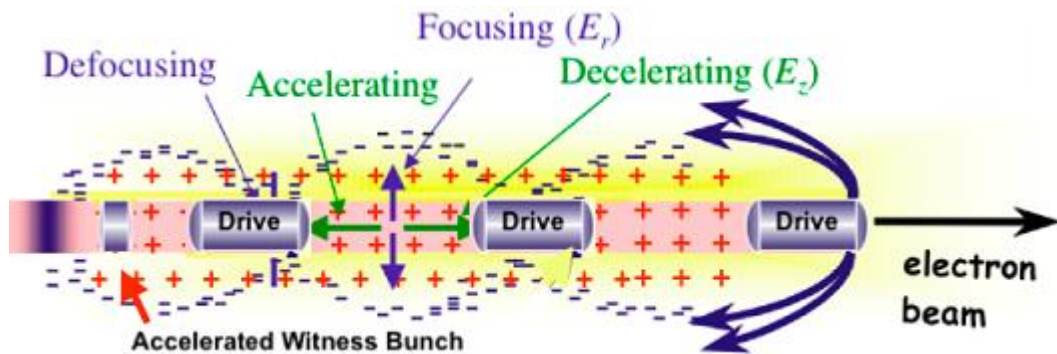


Figure 3.3: Multi-bunch excitation of a plasma wave. A train of injected electron bunches, the *drivers*, creates the plasma wave that accelerates another injected bunch, the *witness*. Every driver blows out the plasma electrons which snap back towards the axis behind the beam. This creates an electron bubble which surrounds the beam that creates it. The electrical field inside the bubble can be used to accelerate the witness.

In the PWFA, a driver electron bunch is injected into a plasma where it transfers energy by expelling the mobile plasma electrons, driving a decelerating field across itself, and therefore experiencing a longitudinally varying retarding potential. After the passage of the drive bunch, the expelled plasma electrons are attracted back by the space charge force of

the immobile massive plasma ions. The ions columns actually is setting up an accelerating field meaning that a witness electron bunch, located in the accelerating field region, can experiences an accelerating potential. Figure 3.4 shows a simplified view of such a process. As the driver and witness bunch are both ultra-relativistic, there is no phase slippage for the particles sampling the wake.

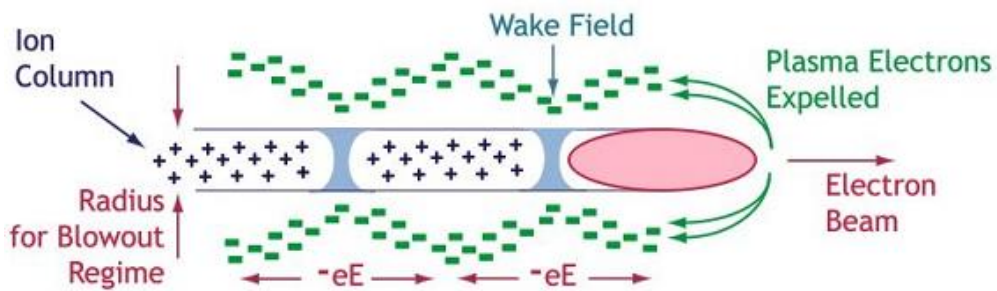


Figure 3.4: Electron Wake schematic view. An electron bunch expels the plasma electrons creating an ion column with focusing and accelerating electric fields.

3.3.1 Regimes in a PWFA

The PWFA is in principle a transformer because the energy lost by the driver bunch (or bunches) is gained by the witness one. When a drive beam, with a density n_b , traverses the plasma, with a density n_0 , occur several regimes depending on their densities. Schematically we have:

$$\begin{cases} n_b < n_0 & \text{Linear regime} \\ n_b \gg n_0 & \text{Non linear (or Blow out) regime} \end{cases}$$

The *linear regime* of the PWFA, where $n_b < n_0$, is characterized by small density modulations in the plasma charge density and very small plasma electron velocities. Using a narrow bunch ($k_p \sigma_z = \sqrt{2}$ and $k_p \sigma_r \ll 1$) with a constant longitudinal profile, the scaling of the wake amplitude in the linear regime is determined, yielding [75]:

$$E_{z,max} \approx 1.3 \frac{m_e c \omega_p}{e} \frac{n_b}{n_0} k_p^2 \sigma_r^2 \ln \frac{1}{k_p \sigma_r} \quad (3.8)$$

where σ_r is the bunch driver spot size and in this case $k_p = \sqrt{2}/\sigma_z$. The linear wakefield response is therefore linear in n_b , but this value can't exceed n_0 .

In the *non-linear regime* $n_b \gg n_0$, the plasma electrons are all swept out of the bunch volume, allowing for the formation of an electron-free, positively charged 'bubble' structure in the shocked plasma. The maximum accelerating field in this regime is [76]:

$$E_{z,max} \approx 1.3 \frac{m_e c \omega_p}{e} \frac{n_b}{n_0} k_p^2 \sigma_r^2 \ln \frac{1}{\left(\frac{n_b}{n_0} k_p^2 \sigma_r^2\right) / 10} \quad (3.9)$$

In this configuration, beam electrons experience simultaneously focusing fields with radial force [77]:

$$F_r \cong -2\pi e^2 n_0 r \quad (3.10)$$

and accelerating longitudinal fields uniform in radius $\partial_r F_z \cong 0$. As a drawback to these distinct advantages, since non-linear plasma response leads to electron relativistic velocities, the wakefield wavelength λ_p becomes amplitude dependent producing a large wave-breaking spike on the first oscillation behind the beam driver. These latter features represent clear limitations for optimal acceleration, in particular to assure a stable resonant plasma response over large distances.

To overcome these limitations, a *quasi – nonlinear regime (QNL)* has been proposed [78] to retain important linear aspects, in particular a constant wavelength to keep resonance conditions, even in a blowout configuration. This is the regime in which the COMB experiment preferably will work (it will depend by the plasma and bunch densities chosen). The key parameter to measure nonlinearity of the plasma response has then identified by the dimensionless charge quantity \tilde{Q} defined as the number of beam electrons normalized to the number of plasma electrons located in a cubic plasma skin depth $k_p^{-1} = c/\omega_p$ [79]:

$$\tilde{Q} \equiv \frac{N_b k_p^3}{n_0} = 4\pi k_p r_e N_b \quad (3.11)$$

A QNL regime is characterized by the condition $\tilde{Q} < 1$ for linearity combined to $\frac{n_b}{n_0} > 1$ for bubble formation. Since optimal conditions for a linear response is based on $k_p \sigma_z \cong \sqrt{2}$, a QNL regime thus requires very thin

beams $\sigma_r \ll \sigma_z$. In this parameter range, linear relations for the wakefield longitudinal field E_z can be extended, up to a limiting value of the n_b/n_0 ratio, where wave breaking $E_z \cong E_0$ occurs. Away from the wave-breaking limit, the analytical relation quoted in [75] gives the same maximum accelerating field $E_{z,max}$ of equation 3.8.

Concluding schematically, regimes for PWFA are:

$$regime = \begin{cases} \text{Linear:} & n_b < n_0 \text{ and } \tilde{Q} \ll 1 \\ \text{Non linear (or Blow out):} & n_b \gg n_0 \text{ and } \tilde{Q} > 1 \\ \text{Quasi non - linear:} & n_b > n_0 \text{ and } \tilde{Q} < 1 \end{cases} \quad (3.12)$$

3.3.2 Matching conditions in a Plasma Accelerator

The aim of this thesis is to study the optic of the SPARC_LAB's linac in order to achieve the matching conditions between electrons bunch and plasma. In this paragraph will see a model [80] to calculate this conditions for a bunch witness in a PWFA.

The concepts developed for the beam transport in the Chapter 2 can be applied in a straightforward way for the case of a plasma accelerator [81] giving important information about the critical topic of beam-plasma matching conditions. To this end we introduce a simplified model for the plasma and for the resulting fields acting on the beam in order to be able to write an envelope equation for the accelerated beam.

We are interested in the case of external injection of particles in a plasma wave, that could be excited by a short intense laser pulse [81,82] or by a driving electron beam [83,84] with beam density n_b near to the plasma density n_0 , $n_b > n_0$. A very simplified model for the plasma behind the

driving pulse is illustrated in Figure 3.5. We will consider a spherical uniform ion distribution, as indicated by a dashed circle, with particle density n_0 . This model is justified by the fact that in this regime the fields are linear in longitudinal and transverse directions, at least in the region of interest for particle acceleration, as the one produced by a uniform ion distribution within a sphere of radius $R_{sphere} \approx \frac{\lambda_p}{2}$ where:

$$\lambda_p = 2\pi c \sqrt{\frac{\epsilon_0 m}{n_0 e^2}} \quad (3.13)$$

is the plasma wavelength. A more detailed treatment [75] shows that the correct scaling is $R_{sphere} = 2\sigma_r \sqrt{\frac{n_b}{n_0}}$, where σ_r is the driving beam rms radius, that for a uniform cylindrical driving bunch gives $R_{sphere} = \frac{\lambda_p}{2} \sqrt{\frac{4eI}{\pi^3 m c^3 \epsilon_0}}$.

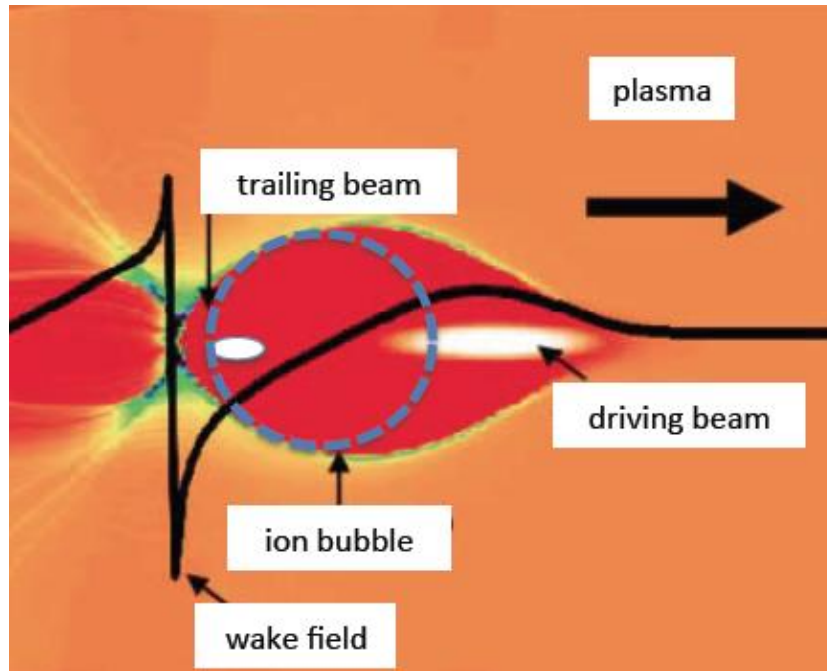


Figure 3.5: Schematic representation of the longitudinal wake field (black line) and ion distribution (red area) behind a driving laser or particle beam [83].

The field produced by the ions and experienced by a witness electron beam is purely electrostatic, being the ions at rest in the laboratory frame on the time scale of interest, and is simply given by:

$$E_r = \frac{en_0}{3\epsilon_0} r \quad (3.14)$$

i.e. it has a radial symmetry (other authors, see for example [83], consider a uniform charged cylindrical ion column producing a transverse field of the form $E_r = \frac{en_0}{2\epsilon_0} r$). The ion sphere is “virtually” moving along z with the speed β_d of the driving pulse due to the plasma electron collective oscillation, even

if the source of the field remains at rest in the laboratory frame. There are also magnetic fields produced by the plasma electron displacement but, as shown in [85], the net effect on a relativistic beam is negligible.

The accelerating component of the field is linearly increasing from the moving sphere center $z_c = \beta_d ct$:

$$E_z(\zeta) = \frac{en_0}{3\epsilon_0} \zeta \quad (3.15)$$

where $\zeta = z - z_c$, and has a maximum on the sphere edge at $\zeta = \frac{\lambda_p}{2}$. The corresponding energy gained by a witness electron is given by $\gamma = \gamma_0 + \alpha L_{acc}$ where L_{acc} is the accelerating length in the plasma and $\alpha(\zeta) = \frac{eE_z(\zeta)}{mc^2} = \frac{1}{3} \left(\frac{2\pi c}{\lambda_p} \right)^2 \zeta$ is the normalized accelerating gradient.

The energy spread accumulated by a bunch of finite rms length σ_z is given by:

$$\frac{\delta\gamma}{\gamma} = \frac{\delta\alpha L_{acc}}{\gamma_0 + \alpha L_{acc}} \approx \frac{\delta\alpha}{\alpha} = \frac{\sigma_z}{\lambda_p} \quad (3.16)$$

showing that ultra-short electron bunches are required to keep energy spread below 1%. In this simplified model beam loading effects are not considered as well as beam slippage with respect to the driving pulse.

The transverse (focusing) field:

$$E_x = \frac{en_0}{3\epsilon_0} x \quad (3.17)$$

at a distance x off the propagation axis is independent of ζ so that correlated emittance growth is not typically induced by the ion focusing field.

In Figure 3.6 are shown the plasma wavelength and the longitudinal and transverse fields experienced by a test particle located at $x = 1 \mu\text{m}$ and $\zeta = \lambda_p/4$ versus typical plasma densities, according to equations 3.69 and 3.70.

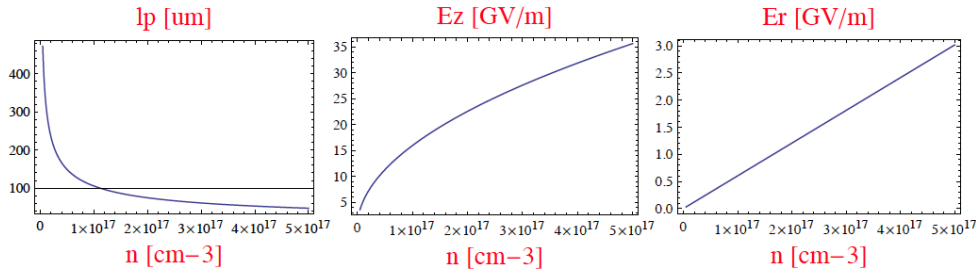


Figure 3.6: Plasma wavelength (left), longitudinal (center) and transverse (right) fields versus typical plasma densities experienced by a test particle located at $x = 1 \mu\text{m}$ and $\zeta = \lambda_p/4$.

As discussed in the previous sections the transverse beam dynamics can be conveniently described by means of a proper envelope equation, to this end let us consider the single particle equation of motion:

$$x'' = \frac{F_x}{\beta c p} = \frac{e^2 n_0}{3\epsilon_0 \gamma m c^2} x = \frac{k_p^2}{3\gamma} x \quad (3.18)$$

where $k_p = \sqrt{n_0 e^2 / \epsilon_0 m c^2}$ is the plasma wave number. The moment of the force acting on the beam particles is given by:

$$\langle x x'' \rangle = \frac{k_p^2}{3\gamma} \langle x^2 \rangle = \frac{k_p}{3\gamma} \sigma_x^2 \quad (3.19)$$

Inserting 3.19 in the envelope equation 2.25 we obtain:

$$\sigma_x'' + \frac{\gamma'}{\gamma} \sigma_x' + \frac{k_p^2}{3\gamma} \sigma_x = \frac{\epsilon_n^2}{\gamma^2 \sigma_x^3} + \frac{k_0^{sc}}{\gamma^3 \sigma_x} \quad (3.20)$$

An equilibrium solution of the previous equation has not yet been found, nevertheless some simplification is still possible and an approximated matching condition exists. As one can see there are two focusing terms: the adiabatic damping and the ion focusing, and two defocusing terms: the emittance pressure and the space charge effects. To compare the relative importance of the first two terms is more convenient to rewrite the previous equation with the new variable $\tilde{\sigma}_x = \sqrt{\gamma} \sigma_x$ leading to the equation:

$$\tilde{\sigma}_x'' + \left(\left(\frac{\gamma'}{2\gamma} \right)^2 + \frac{k_p^2}{3\gamma} \right) \tilde{\sigma}_x = \frac{\epsilon_n^2}{\tilde{\sigma}_x^3} + \frac{k_0^{sc}}{\gamma^2 \tilde{\sigma}_x} \quad (3.21)$$

The beam is space charge dominated (defocusing regime, as already discussed in the paragraph 2.3.5) when:

$$\rho = \frac{k_0^{sc} \tilde{\sigma}_x^2}{\varepsilon_n^2 \gamma^2} = \frac{k_0^{sc} \sigma_x^2}{\varepsilon_n^2 \gamma} \gg 1 \quad (3.22)$$

and ions focusing dominated when:

$$\eta = \frac{4\gamma k_p^2}{3\gamma'^2} \gg 1 \quad (3.22)$$

With the typical beam parameters of the COMB experiment: $I = 581.4$ A, $\varepsilon_n = 0.66$ μ m, injection energy $\gamma = 300$ and spot size about 8 μ m, we have $\rho < 1$ and $\eta > 1$. It follows that the envelope equation can be well approximated by the following reduced expression:

$$\sigma_x'' + \frac{k_p^2}{3\gamma} \sigma_x = \frac{\varepsilon_n^2}{\gamma^2 \sigma_x^3} \quad (3.23)$$

with $\gamma(z) = \gamma_0 + \alpha z$. Looking for a particular solution in the form $\sigma_x = \gamma^{-1/4} \sigma_0$ we obtain:

$$\left(\frac{5}{16} \gamma'^2 + \frac{1}{3} \gamma k_p^2 \right) \sigma_0 = \frac{\gamma \varepsilon_n^2}{\sigma_0^3} \quad (3.24)$$

that for $\eta > 1$ has a simple solution $\sigma_0 = \sqrt{\frac{\sqrt{3}\epsilon_n}{k_p}}$ giving the matching condition of the beam with the plasma:

$$\sigma_x = \gamma^{-1/4} \sigma_0 = \sqrt[4]{\frac{3}{\gamma}} \sqrt{\frac{\epsilon_n}{k_p}} \quad (3.25)$$

In Figure 3.7 are shown the matched beam envelope given by equation 3.25 with normalized emittance of $2 \mu m$ and injection energy $\gamma = 300$ versus the plasma density. In the same figure is shown also the evolution of the beam envelope in a 10 cm long plasma with density 10^{16} cm^{-3} , corresponding to an accelerating field of 5 GV/m (extraction energy $\gamma = 1300$) and focusing field of 60 MV/m .

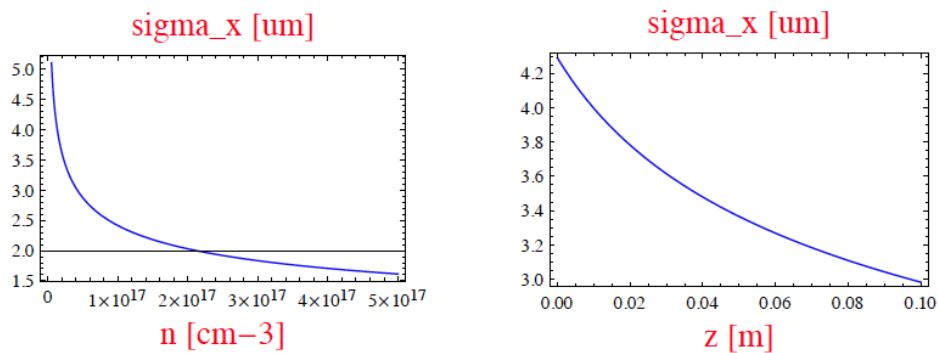


Figure 3.7: Matched beam envelope with normalized emittance of $2 \mu m$ and injection energy $\gamma = 300$ versus the plasma density (right) and the evolution of the beam envelope in a 10 cm long plasma with density

10^{16} cm^{-3} , corresponding to an accelerating field of 5 GV/m and focusing field of 60 MV/m .

Notice that the beam experiences focusing as γ increases and the beam density increases leading to a significant perturbation of the plasma fields. A possible solution to overcome this effect is to taper the plasma density along the channel in order to achieve beam transport with constant envelope.

On the other hand before injection in the plasma accelerator, the beam has to be focused to the matching spot given by equation 3.25 to prevent envelope oscillations that may cause emittance growth and an enhancement of betatron radiation emission. It has been proposed [31] to shape the plasma density profile in order to gently capture the beam by means of the increasing ion focusing effect.

3.4 Chapter conclusions

As reported in the Chapter, in a plasma accelerator the electrons need to be trapped by the plasma wave that, both in laser and beam-driven case, can be linear or nonlinear, but the wakefield must not exceed the cold wave breaking field. In the self-injection schemes, the plasma background electrons are trapped and accelerated, i.e. the plasma acts as the accelerating structure and the electron source. The drawback of this method is that the instant of the injection cannot be controlled accurately and the self-injection continues while the driver propagates through the plasma. For example, in the early laser-driven experiments, this led to an

energy spread of 100% with rather poor shot-to-shot reproducibility. Smaller values can be reached at the price of a lower number of accelerated particles. A similar behaviour has been observed for PWFA, where the first achieved experiment used a long driver bunch in which the electrons located in the tail gained energy at the expense of the ones in the head. Later experiments demonstrated the feasibility in using multi-bunches schemes, resulting in the most promising plasma-based technique to reach very high energies through the use of the staging.

For both methods to have a future in applications, electron bunches with high reproducibility, consistent energy and low energy spread are required, therefore self-injection schemes are not adequate. An external electron source in combination with a plasma channel would therefore be most desirable. Since a radio frequency (RF) photo-injector is one of the brightest pulsed electron sources with high peak current, this is the best candidate to serve as external injector. In this context chapter 4 is dedicated to simulations, of the COMB experiment at SPARC_LAB studying the optic of the bunch in order to achieve the matching conditions between bunch and plasma.

Chapter 4

Numerical simulations

In this chapter the set-up of the interaction chamber for the COMB experiment and the numerical simulation results of electron beam to be injected in to the plasma will be presented. By means of the General Particle Tracer (GPT) code, a well-established simulation platform for the study of charged particle dynamics, a numerical simulation for the SPARC_LAB's linac starting from the cathode up to the injection in to the plasma capillary has been implemented. In particular the magnetic layout has been analyzed. To achieve the matching conditions of equation 3.78 several magnetic elements (consisting in quadrupoles and solenoids) along the beam line have been inserted.

4.1 General Particle Tracer (GPT)

The General Particle Tracer (GPT) code is a completely 3D code and includes various space-charge models, ranging from 1D interaction to fully 3D point-to point calculations and allowing to investigate the non-linear effects of charged particles dynamics in electromagnetic fields by using an embedded fifth order Runge-Kutta driver with adaptive step-size control that ensures accuracy while keeping the computation time to a minimum. Almost all standard accelerator components are represented in GPT by specific sub-routines. Moreover, to achieve the full modelling of some components, the

code is able to handle external field maps generated with other codes, like SUPERFISH [86].

Regarding the space-charge calculation, GPT has a number of built-in elements to calculate Coulomb interactions, each of which is optimized for a different application. All routines in GPT dealing with Coulomb interactions are derived from the electric field at the position of particle i due to Coulomb interaction with all particles j , i.e.

$$E_i = \sum_{i \neq j} \frac{q_j}{4\pi\epsilon_0} \cdot \frac{r_j - r_i}{|r_j - r_i|^3} \quad (4.1)$$

Space charge is usually defined as the particles collective effect, it is governed by long-range interactions with charge density. The summation hereby changes into an integration. This implies a smooth, fluid-like charge distribution, where the point-like nature of charge can be ignored. In that case, assuming the electrostatic case only, Coulomb interactions can be rewritten in terms of Poisson's equation:

$$-\nabla^2 V = \frac{\rho}{\epsilon_0} \quad (4.2)$$

where ρ is the charge density and V the electrostatic potential. This equation is numerically much easier to solve compared to the previous point-to-point calculation of equation 3.1, but it is not correct in the case where granularity or stochastic effects play a dominant role. The simulation described uses the **spacecharge3Dmesh** routine, based on solving Poisson's

equation in 3D in the rest frame of the bunch by dividing the total beam in N macro-particles. It is by far the fastest space-charge model in the GPT code because it scales as $O(N)$ in terms of CPU time and a single Lorentz transformation is used to convert the calculated electrostatic fields in the co-moving frame into both electric and magnetic fields for the tracking engine.

4.2 The GPT executable

A schematic of the GPT executable is shown in the figure below. The following paragraph describes the individual components in detail.

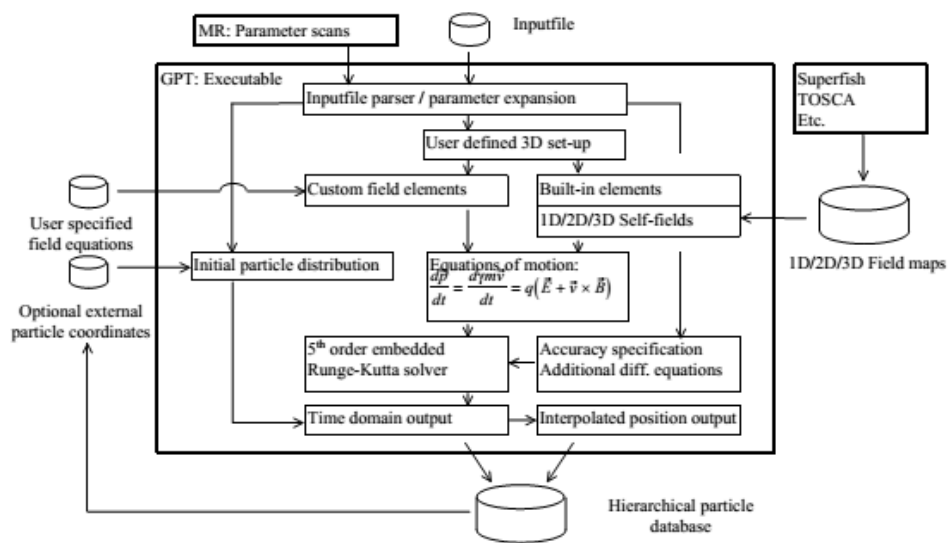


Figure 4.1: Schematic representation of the GPT executable.

The GPT executable starts by reading one (or more) ASCII inputfile(s) describing the simulation to perform. The inputfile specifies the initial particle distribution, the 3D electromagnetic field configuration (set-up),

the required accuracy of the calculations and the output method. Standard expressions, functions and user-defined variables can be used for convenience. Optionally, a MR file (Multiple Run) can be used to automatically scan any number of parameters. The initial particle distribution consists of a number of macro-particles, each typically representing a large number of elementary particles.

The set-up defines the 3D electromagnetic field configuration as generated by the beam-line components. It can be composed of any number of built-in elements, external 2D or 3D field maps and user-defined expressions in custom elements.

GPT has two available output modes: time and position output. Time output writes all particle coordinates at user defined times. Position output writes all particle coordinates passing any plane in 3D space. Optionally, the electric and magnetic fields at the particle coordinates are also saved, which greatly helps in understanding particle dynamics.

GPT is accompanied by a number of pre- and post-processing programs as well as interfaces to other software packages. The typical data flow within GPTwin is shown in Figure 4.2.

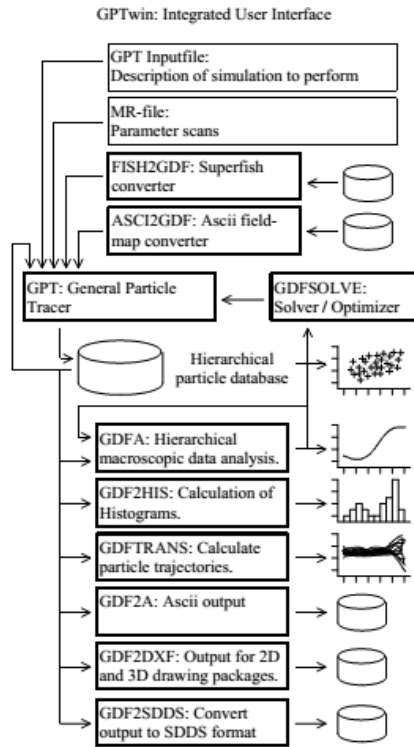


Figure 4.2: Typical data flow within GPT.

The GPT results are saved in to a binary file, written in the General Datafile Format (GDF), for off-line analysis and interpretation. This file allows the post-processing components to easily extract information and, as shown in Figure 4.2, various conversion utilities are available to convert to and from the GDF format.

The main analysis program for GPT output is GDFA; it calculates macroscopic beam parameters as function of simulation time, position or any scanned parameter. So typical macroscopic quantities like emittance, bunch length, average energy and beam radius can be obtained.

The MR and GDFSOLVE utilities can be used to run a sequence of simulations with one or more parameters varying. The MR program scans over a pre-defined multi-dimensional parameter range while GDFSOLVE automatically optimizes a design until user-defined criteria (constraints) are met.

4.3 Linac start to end simulation

This section describes the simulation layout used to reproduce the experimental data of the SPARC_LAB's linac. The set up of the experiment is shown in Figure 4.3.

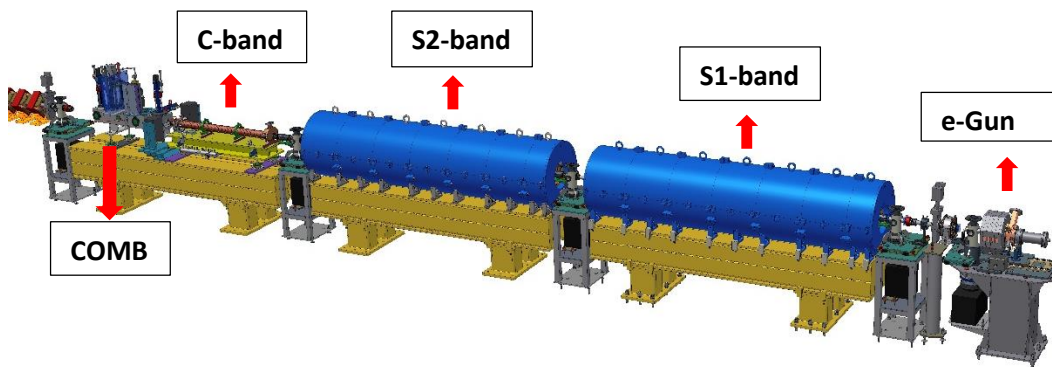


Figure 4.3: SPARC_LAB linac and the COMB vacuum chamber.

The first two S-band structures are assumed working at the frequency of $f = 2.856 \text{ GHz}$, that is the frequency of conventional S-band structures, while the C-band has a frequency of $f = 5.712 \text{ GHz}$.

- The simulation starts by modelling the e-gun. A field map of the cavity, containing the values of the radial and longitudinal electric fields (E_r, E_z) together with the azimuthal magnetic field (B_ϕ), is imported by using the **map25D_TM** routine. The particle acceleration is performed assuming $E_z \sim \cos(2\pi ft - kz + \phi)$; choosing $\phi = 30^\circ$ as injection phase, the modelled e-gun is able to reproduce the expected 5.6 MeV exit kinetic energy, with longitudinal peak fields of about 120 MV/m .

- A solenoid, at the e-gun exit is reproduced by importing a $2D$ magnetic field map containing the radial and longitudinal magnetic fields with the **map2D_B** routine. The solenoid consists of four separated coils: to obtain a vanishing rotation angle, the coils have been powered in couples by opposite currents. This configuration does not affect the focusing power which depends on the square of the magnetic field, that is of the order of 3 kG .
- The two S-band sections (about 3 m long) that constitute the first linac's part are schematized by the **trwlinac** routine. They (S1, starting at $z_{start}(S1) = 1.54\text{ m}$ and S2, at $z_{start}(S2) = 5.14\text{ m}$) provide about 20 MV/m accelerating fields. By considering an input energy of 5.6 MeV , they allow to reach final energies up to 125 MeV .
- Solenoid coils around the first two sections provide a magnetic field of the order of 0.7 kG . They can be powered to provide additional magnetic focusing to better control the beam envelope and the emittance oscillations under RF compression. They are schematized importing a $2D$ magnetic field maps containing the radial and longitudinal magnetic fields with the **map2D_B** routine.
- The new C-band section (1.4 m long) is located after the two S-band. It ($z_{start}C = 8.74\text{ m}$) is able to achieve an accelerating field as high as 35 MV/m , so it allows to reach final energies up to 180 MeV . The C band is schematized by the **trwlinac** routine.

4.4 Ultrashort and low emittance bunch simulation

As shown in the previous chapter for a plasma acceleration experiment an ultrashort electron bunch is required, therefore a compression in the velocity bunching mode is needed at SPARC_LAB (see section 2.4). Moreover in order to keep under control the emittance growth, it is also necessary to use the solenoid around S1. The initial beam dynamics is regulated by the following assumptions:

- To simulate the particle release by the photo-cathode, the UV laser hitting the cathode surface consists of a pulse with Gaussian temporal profile ($\sigma_t = 60 \text{ fs rms}$). Also the laser transverse profile is assumed to be uniform, with a radius of $380 \mu\text{m rms}$.
- The bunch (witness) charge is $Q_{tot} = 25 \text{ pC}$.
- By assuming a 4.66 eV UV laser (corresponding to $\lambda = 266.7 \text{ nm}$), the electrons released by the photo-cathode have an initial energy of 0.36 eV . At this stage the bunch structure is assumed to be the same of the laser generating it, both longitudinally and transversally.

The evolution of the emitted particles depends on different machine component settings. At simulation time the beam has to be characterized by its *on crest* configuration, i.e. the machine settings giving the higher output energy. This configuration set the on crest phases of the three TW sections ($\varphi_{S1,crest}, \varphi_{S2,crest}, \varphi_{C,crest}$). At this point, the longitudinal beam profile can be controlled by changing the phase of both the e-gun and S1.

Once the longitudinal profile is defined, the transverse one and the beam emittance are controlled mainly by the gun-solenoid and S1-solenoid. The parameters set in the simulation are:

- The gun phase is fixed at $\phi_{gun} = 30^\circ$ that corresponds to a kinetic energy $E_{gun} = 5.6 \text{ MeV}$.
- The S1 phase is at -89.9° with respect to $\varphi_{S1,crest}$. It sets the simulated bunch longitudinal lengths after S1 at $\sigma_z = 13 \mu\text{m}$ (i.e. about 40 fs).

In Figure 4.4 and Figure 4.5 the bunch space phase before and after S1-band compression is shown.

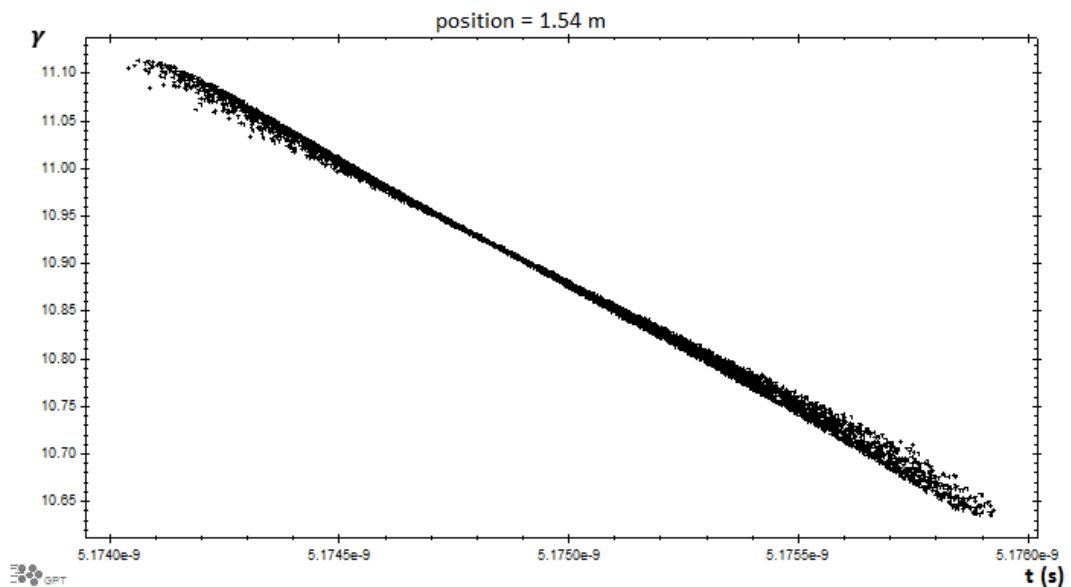


Figure 4.4: Phase space at $z = 1.54 \text{ m}$ before S1 band. In the y axis there is the Lorentz factor γ .

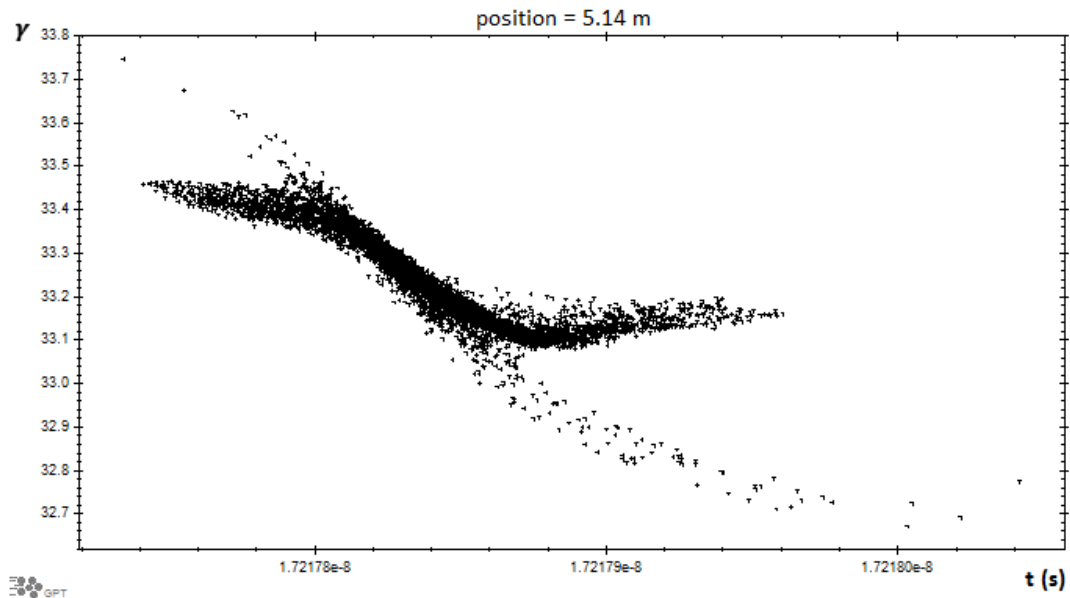


Figure 4.5: Phase space at the entrance of S2-band, $z = 5.14 \text{ m}$. Velocity bunching reduces the longitudinal profile from $154 \mu\text{m}$ to $13 \mu\text{m}$, with a compression factor > 10 .

- The S2 phase is set on crest at the value of $\varphi_{S2,crest}$, so S2-band provides the maximum energy at the bunch leaving almost unchanged the longitudinal profile.

Figure 4.6 shows the longitudinal bunch profile at the entrance of C-band.

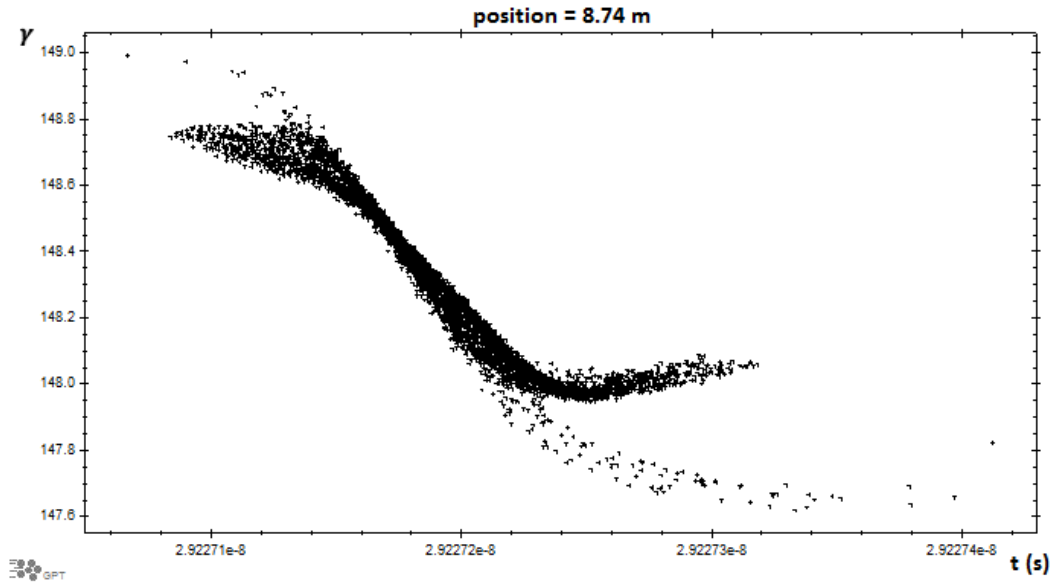


Figure 4.6: Phase space at the entrance of C band $z = 8.74 \text{ m}$, the longitudinal profile is almost the same as in Figure 4.4.

- The C-band phase is set on crest at the value of $\varphi_{C,crest}$. The final beam energy at the exit of C-band is 123 MeV ($\gamma = 247$).

Figure 4.7 shows the beam energy and the beam longitudinal profile along the linac. Working on velocity bunching mode S1 reduces the longitudinal bunch length. The energy increase across the three accelerating sections is clearly visible, the higher slope across C-band denotes a higher gradient. The lower slope of the energy growth, across S1-band compared to S2-band, denotes that S1 is not working on crest but in the velocity bunching mode. The small deceleration in the first part of S1-band is due to the compression process, in which the bunch head is decelerated compared to the tail.

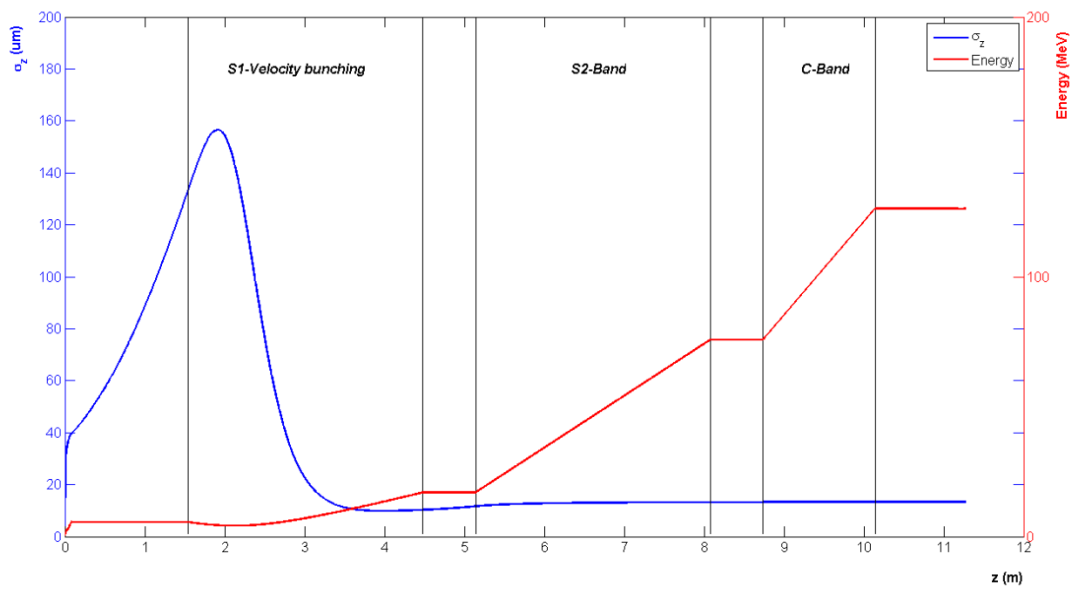


Figure 4.7: Courses of the energy and longitudinal profile σ_z of the bunch across the linac. S1 starts from $z_{S1,start} = 1.54 \text{ m}$ ends at $z_{S1,end} \sim 4.54 \text{ m}$, S2 starts from $z_{S2,start} = 5.14 \text{ m}$ ends at $z_{S2,end} \sim 8.14 \text{ m}$, C starts from $z_{C,start} = 8.74 \text{ m}$ ends at $z_{C,end} \sim 10.14 \text{ m}$.

Figure 4.8 shows the courses of the energy and the energy spread across the three accelerating sections. Energy spread is below 0.15%.

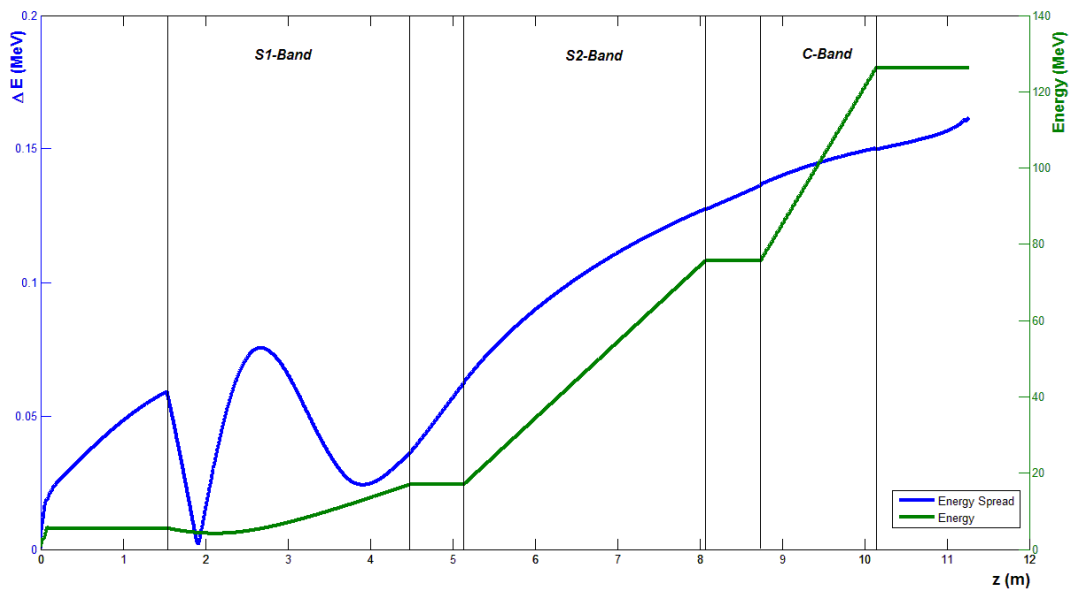


Figure 4.8: Energy and energy spread across the linac.

To compensate the emittance growth, as already discussed, the gun-solenoid and S1-solenoid can be used. The currents for S1-solenoid and for gun-solenoid were found by a phase scan with GPT Multiple Run technique in order to minimize the final emittance.

- The gun-solenoid provide a magnetic field of 2.5 *kG*.
- The best final emittance value has been obtained providing a magnetic field of 513 *G* with the solenoid coils around S1 section.

Through the emittance compensation technique the simulated normalized emittance before the plasma decrease to $\varepsilon_{n,rms} = 0,66 \mu m$.

4.5 The COMB interaction chamber

In order to start the COMB experiment, an interaction chamber (see Figure 4.9 and Table 4.1 and Table 4.2 for the lengths and distances relevant for these simulations) has been designed and realized and it will be positioned after the C-band; therefore the electrons bunches will enter in the interaction area with an energy of about 123 *MeV*, with the linac operating in velocity bunching mode.

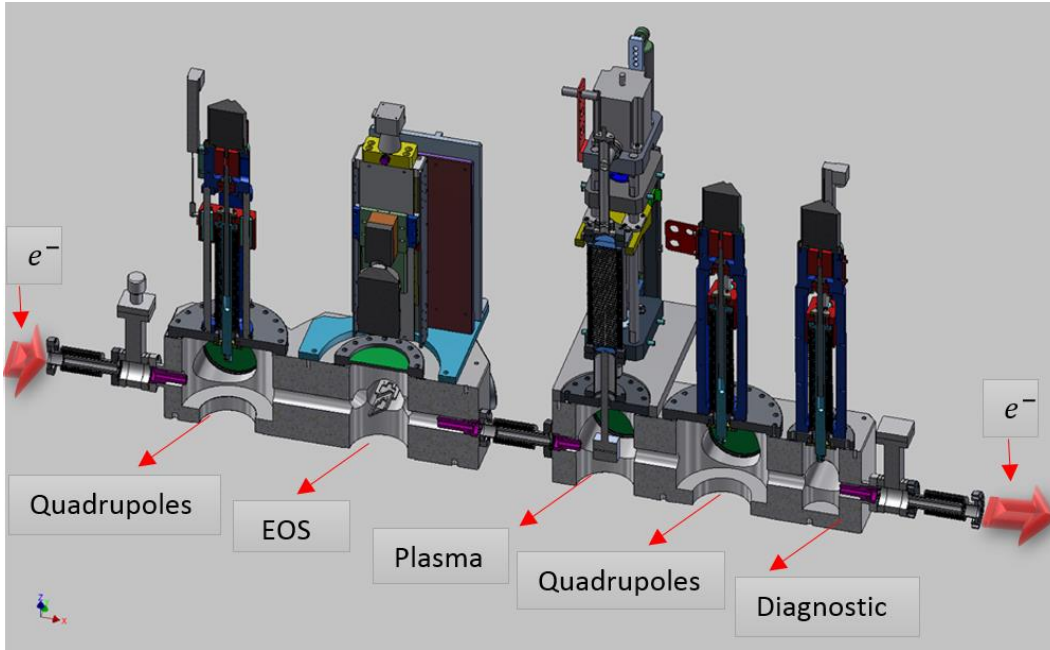


Figure 4.9: The COMB interaction chamber with the five vacuum sub-chambers.

In the first vacuum sub-chamber a triplet of permanent quadrupoles will be placed in order to focus the electrons before the plasma, in order to respect the matching conditions between electrons and plasma. In the second vacuum sub-chamber there will be a longitudinal beam diagnostics based on Electro-Optic Sampling (EOS), the third space is for the plasma capillary. In the fourth space there will be another triplet of permanent quadrupoles with the aim of capturing the bunch at the exit of the plasma accelerator. The last vacuum sub-chamber is reserved for transverse beam diagnostics.

Chamber	Length
Quadrupoles before plasma	15,6 cm
EOS Diagnostics	10 cm
Plasma capillary	10 cm
Quadrupoles at plasma exit	15,6 cm
Transverse diagnostics	6,3 cm

Table 4.1: Vacuum chambers dimensions

Distances between:	Distance
End of C band – Centre of the first quadrupoles chamber	45,8 cm
Centre of the first quadrupoles chamber – Centre of the plasma chamber	64,8 cm
Centre of the plasma chamber - Centre of the second quadrupoles chamber	20 cm

Table 4.2: Relevant distances for the COMB experiment

4.6 Matching conditions at SPARC_LAB

Before set up the magnetic elements, calculate the matching conditions to achieve:

$$\sigma_x = \gamma^{-1/4} \sigma_0 = \sqrt[4]{\frac{3}{\gamma}} \sqrt{\frac{\varepsilon_n}{k_p}} \quad (4.3)$$

in the case of the COMB experiment.

The value of γ and ε_n (respectively the bunch Lorentz factor and the normalized rms emittance at the plasma entrance) are fixed to $\gamma = 247$ and $\varepsilon_n = 0.66 \mu\text{m}$, as obtained by the GPT simulations. Two interesting plasma configurations and parameters for the COMB experiment are shown in Table 4.3 according to two possible configurations for the plasma densities: $n_0 = 10^{15} \text{cm}^{-3}$ and $n_0 = 10^{16} \text{cm}^{-3}$. Those lead to two different values for the plasma wavelength λ_p and the plasma wave number k_p .

Densities	$\lambda_p(\mu\text{m}) \approx \frac{3.3 \times 10^{10}}{\sqrt{n_0}}$	$\sigma_{x,max}(\mu\text{m})$
$n_0 = 10^{15} \text{cm}^{-3}$	≈ 1043.6	3.50
$n_0 = 10^{16} \text{cm}^{-3}$	≈ 330	1.97

Table 4.3: Relevant values to calculate matching conditions at two different plasma densities of $n_0 = 10^{15} \text{cm}^{-3}$ and $n_0 = 10^{16} \text{cm}^{-3}$.

In Figure 4.9 the matching conditions with the COMB parameters are shown, on the x axis the plasma density n_0 varies from a value of $n_0 = 10^{15} \text{cm}^{-3}$ to a value of $n_0 = 10^{16} \text{cm}^{-3}$.

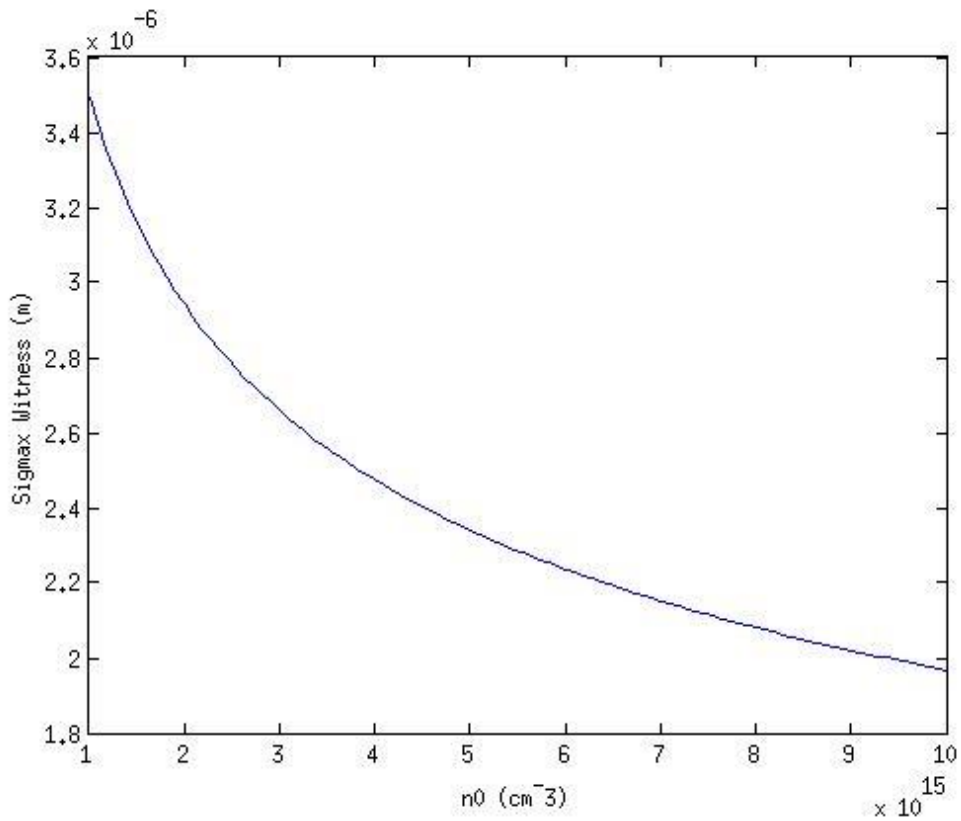


Figure 4.10: On the y axis there are the matching conditions plotted through the model presented in paragraph 3.3.2, on the x axis the plasma density n_0 varies from a value of $n_0 = 10^{15} \text{cm}^{-3}$ to a value of $n_0 = 10^{16} \text{cm}^{-3}$.

For a density of $n_0 = 10^{16} \text{cm}^{-3}$ we have a $\sigma_{max} = 1.97 \mu\text{m}$ while for a density of $n_0 = 10^{15} \text{cm}^{-3}$ we have a $\sigma_{max} = 3.50 \mu\text{m}$.

4.7 Insertion of magnetic elements before plasma

In order to achieve the previous matching conditions between bunch and plasma, two triplets of quadrupoles have been inserted through GPT and the S2-solenoid field has been changed. The first triplet is a magnetic one

and is located around the C-band with low gradient ($< 10 T/m$), while the second one is composed by a high gradient ($< 500 T/m$) permanent quadrupoles inside the interaction chamber before plasma.

- The S2-solenoid has been searched by a scan with GPT Multiple Run, therefore it has been optimized through GDFSOLVE in order to minimize the final spot-size. The best final spot-size value was obtained with a magnetic field of 1 *kG*.
- In order to find the positions and reasonable gradients for the quadrupoles located around the C band, in a speedy way, a GPT Multiple Run (MR) has been used first leading to coarse values. Secondly, through the GPT tool **GDFSOLVE**, a better configuration scheme has been defined in order to achieve the matching conditions. In order to refine the results, GDFSOLVE loops over previous output values until it finds the stables one; the constraint for GDFSOLVE is the beam size at the plasma entrance given by the matching conditions. To simulate the quadrupoles around the C-band, the **quadrupole** routine has been used importing an external field map. In the scan the gradients can vary from 0 *T/m* to 10 *T/m*, the positions and lengths can vary along the C band. The best positions lengths and gradients for the magnetic triplet around the C-band are reported in Table 4.4:

C-Quadrupole	Position (m)	Length (cm)	Gradient (T/m)
Quadrupole 1	$z_{start} = 8.94$	20	-0.49
Quadrupole 2	$z_{start} = 9.21$	20	1.28
Quadrupole 3	$z_{start} = 9.48$	20	-0.818

Table 4.4: Values of the best gradients, positions and lengths of the C-triplet, obtained with GPT Multiple Run and GDFSOLVE.

- This configuration of S2-solenoid current and gradients and positions of triplet around C-band, corresponds to a beam that doesn't enter in permanent triplet with a beam waist (i.e. the beam has $\alpha \neq 0$). For the final spot-size this configuration is better compared to a configuration in which the beam enters in the permanent triplet with a beam waist ($\alpha = 0$). This is explained by a beam that enters in the permanent triplet with a beam waist is too much small and it doesn't experience the magnetic fields of the permanent quadrupoles.
- The positions and gradients for the high gradient permanent quadrupoles inside the COMB interaction chamber have been obtained through the same GPT Multiple Run and GDFSOLVE technique. The results are reported in Table 4.5. To schematize the permanent quadrupoles the **quadrupole** routine has been used; in the scan the gradients can vary from $0 T/m$ to $500 T/m$, the positions and lengths can vary inside the COMB chamber. The constraint for the GDFSOLVE is the spot size at the plasma entrance, given by the matching conditions.

Permanent	Position (m)	Length (cm)	Gradient (T/m)
Quadrupole 1	$z_{start} = 10.5494$	3	-65.4
Quadrupole 2	$z_{start} = 10.5994$	3	127
Quadrupole 3	$z_{start} = 10.6494$	3	-65.5

Table 4.5: Values of the best gradients, positions and lengths for the permanent triplet inside the COMB chamber, obtained with GPT Multiple Run and GDFSOLVE.

4.8 Final results for the spot size

With the configuration of the magnetic elements shown in the paragraph 4.7, we have the best spot size achievable at SPARC_LAB for the COMB experiment assigned with GPT Multiple Run and GDFSOLVE. We searched for a final cylindrical symmetric beam in which the final spot size along the x and y axis is the same. The best results with this magnetic configuration is $\sigma_x = 8.2 \mu m$ and $\sigma_y = 8.2 \mu m$ that coincide with a beam waist ($\alpha = 0$) at the plasma entrance.

Figure 4.11 shows the trend of the normalized emittance $\varepsilon_{n,rms}$ and the spot size along the x axis σ_x , the minimum for the spot size is at the entrance of the plasma channel.

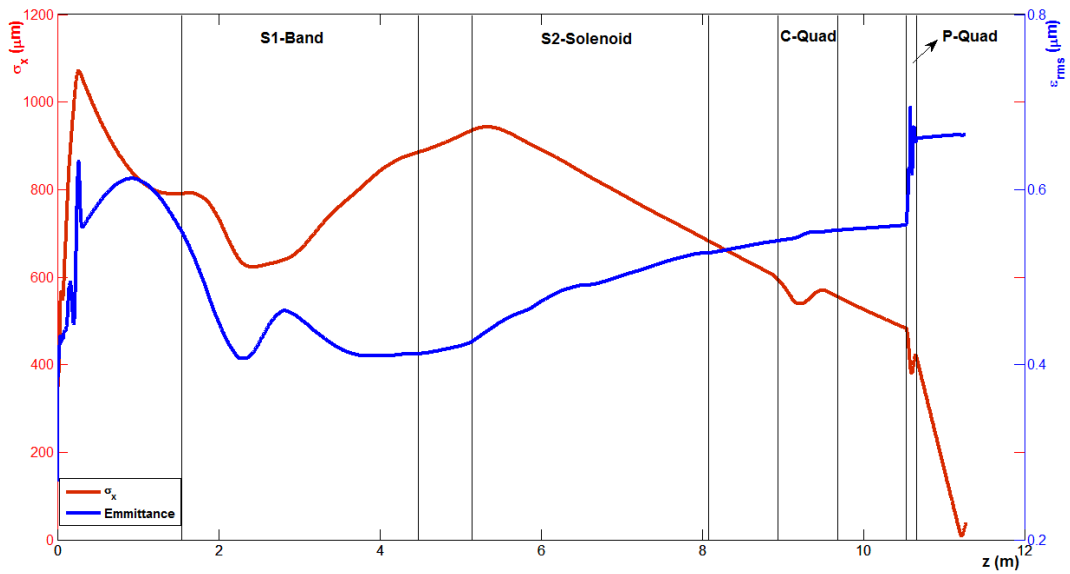


Figure 4.11: Normalized emittance $\varepsilon_{n,rms}$ trend and the spot size along x axis σ_x ; the minimum for the spot size is at the plasma entrance. The growth of the spot size σ_x following the minimum value is due to a drift of 8 cm after the start of the plasma (plasma's influences are not simulated here).

Other appreciable spot sizes have been obtained with the same magnetic configuration of the two triplets by varying the S2-solenoid current only; in this way the beam waist moves along z. For example with a 112.6 A S2-solenoid current, we obtain a convergent beam at the plasma entrance with a spot size of $12\mu m$; in this configuration the beam waist is below 1 cm after the plasma entrance with a spot size of $\sigma_x = 5.8\mu m$ $\sigma_y = 6.24\mu m$. This configuration is convenient to exploit the lens effect of the plasma, availing its transverse focusing field, and it will be use during the COMB experiment.

4.9 Regime for the COMB experiment

As we have seen in section 3.3.1, the COMB experiment will work in the linear regime in which $n_b < n_0$ and $\tilde{Q} \ll 1$, or better in the quasi non-linear regime in which (see 3.67) $n_b > n_0$ and $\tilde{Q} < 1$ in order to retain important linear aspects even in a blowout configuration. Regime depends on the choice of the plasma density inside the capillary. Table 4.6 reports the values for relevant parameters in the COMB experiment, taking into account four driver bunches each one with a charge of 50 pC , a bunch length of $\sigma_z = 30 \text{ }\mu\text{m}$ and a plasma density of $n_0 = 10^{16} \text{ cm}^{-3}$.

Parameters	Values
n_0	10^{16} cm^{-3}
Q_{bunch}	50 pC
Q_{tot}	200 pC
N_b	3.12×10^8
V_b	$2.02 \times 10^{-15} \text{ m}^{-3}$
n_b	$1.55 \times 10^{17} \text{ cm}^{-3}$
λ_p	$333 \text{ }\mu\text{m}$
ω_p	$5.66 \times 10^{12} \text{ s}^{-1}$
k_p	$1.91 \times 10^4 \text{ m}^{-1}$
\tilde{Q}	0.84

Table 4.6: Values for relevant parameters in the COMB experiment assuming four 50 pC driver bunches with a plasma density $n_0 = 10^{16} \text{ cm}^{-3}$. Q_{bunch} is the bunch charge, Q_{tot} is the total charge, N_b is the number of the

electrons in each bunch, V_b is the volume occupied by the bunch and n_b is the bunch density.

Since $\tilde{Q} < 1$ and $n_b > n_0$, it is evident that we are in the quasi non-linear regime.

Considering a plasma density $n_0 = 10^{15} \text{ cm}^{-3}$, in Table 4.7 there are the same values for the parameters for the same four driver bunches.

Parameters	Values
n_0	10^{15} cm^{-3}
Q_{bunch}	50 pC
Q_{tot}	200 pC
N_b	3.12×10^8
V_b	$2.02 \times 10^{-15} \text{ m}^{-3}$
n_b	$1.55 \times 10^{17} \text{ cm}^{-3}$
λ_p	$1053 \text{ }\mu\text{m}$
ω_p	$1.79 \times 10^{12} \text{ s}^{-1}$
k_p	$5.96 \times 10^3 \text{ m}^{-1}$
\tilde{Q}	0.264

Table 4.7: Values for relevant parameters in the COMB assuming four 50 pC driver bunches with a plasma density of $n_0 = 10^{15} \text{ cm}^{-3}$.

Being again $\tilde{Q} < 1$ and $n_b > n_0$, it is evident that also in the case of plasma density $n_0 = 10^{15}$, we are still in the quasi non-linear regime. To be able to exit from the quasi non linear regime and go to the linear regime ($n_b < n_0$)

for the COMB experiment we need to decrease the bunch density below $n_b < 10^{15} \text{ cm}^{-3}$.

4.10 Plasma like a THz cavity

In the COMB experiment the plasma channel will be created in a 5 cm long capillary filled by hydrogen, which will be fully ionized by a discharge. In the COMB chamber another triplet of permanent quadrupoles will be placed after the plasma, in order to capture the bunch and avoid an increase of the spot size. In order to find the gradients of the quadrupoles, a plasma simulation has been performed. Using GPT it is possible to perform a simulation in which the plasma wake, with a density of $n_0 = 10^{16}$, is simulated by an accelerating section with a frequency of 1 THz. In this way only the longitudinal acceleration can be taken into account for the bunch, because in general the transverse focusing field of the plasma cannot be simulated by an accelerating section.

- The longitudinal (accelerating) field in the simulation is the same accelerating field produced by four bunch drivers, everyone with $Q = 20 \text{ pC}$ and $\sigma_z = 30 \text{ }\mu\text{m}$, in a plasma with a density of $n_0 = 10^{16} \text{ cm}^{-3}$, leading to 1 GV/m peak accelerating gradient. The wave breaking in this configuration correspond to $\sim 10 \text{ GV/m}$. The cavity has been modelled by **trwlinac** routine. The results of the simulation have shown that the bunch exiting the plasma channel have a Lorentz factor $\gamma = 341.6$ that correspond to a final energy $E_{final} = 170.3 \text{ MeV}$.

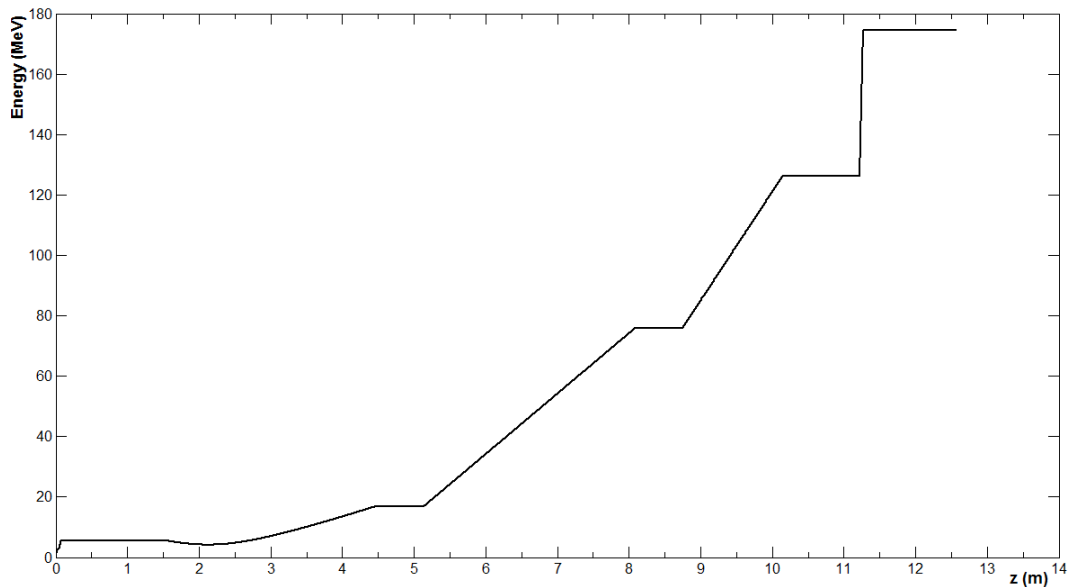


Figure 4.12: Energy along the linac is upgraded with the plasma channel to a value of $E_{final} = 174.6 \text{ MeV}$. Plasma starts at $z = 11.3 \text{ m}$. In the y axis there is the Lorentz factor.

In the COMB chamber another triplet of permanent quadrupoles will be placed after the plasma, in order to capture the bunch and avoid a spot size increase. To find coarse values for this quadrupoles a simulation with GPT Multiple Run and GDFSOLVE has been performed.

- The quadrupoles strength scales like $1/\gamma$ so at the plasma exit there will be majors gradients compared to the precedents. The **quadrupole** routine has been used to model the permanent quadrupoles. Through GPT Multiple Run and GDFSOLVE the best positions, lengths and gradients (from 0 T/m to 500 T/m) has been scanned for this triplet. The constraint used in the simulation is the minimum spot size achievable at the entrance of the successive

triplet in the SPARC _LAB beam line (that is at $z = 12.34\text{ m}$). The optimal position lengths and gradients are reported in Table 4.98.

Permanent After plasma	Position (m)	Length (cm)	Gradient (T/m)
Quadrupole 1	$z_{start} = 11.396$	3	-150
Quadrupole 2	$z_{start} = 11.446$	3	279
Quadrupole 3	$z_{start} = 11.496$	3	-149

Table 4.8: Values of the best gradients, positions and lengths for the permanent triplet inside the COMB chamber after plasma, obtained with GPT Multiple Run and GDFSOLVE in order to have a minimum spot size at a $z = 12.34\text{ m}$.

Conclusions

At the SPARC_LAB test facility a beam driven plasma acceleration experiment named COMB will start in the 2015. Nowadays the COMB interaction chamber has been designed and constructed and it will be installed at the end of the linac where the beam energy is about $E_{final} = 123 \text{ MeV}$. A beam driven plasma acceleration experiment needs an ultrashort electron bunch, so the first S-band accelerating section of the SPARC_LAB linac has to work in velocity bunching mode.

In this thesis with a simple model for the plasma wake excited by the driver bunch, it has been calculated the matching conditions (to preserve the beam quality) between the electron bunch and the plasma. This model schematizes the plasma wake as a spherical ion distribution; the use of this model is justified by the fact that in the regime that we will use during the COMB experiment, the fields are linear in longitudinal and transverse direction at least in the region of interest for the acceleration. The matching conditions scale as $\sqrt{\epsilon_n/n_0}$, so enhancing the plasma density n_0 , the wave breaking field E_0 increase and so, enhancing n_b it is possible to reach a higher accelerating gradient; however, by increasing n_0 , the plasma wavelength λ_p will be smaller, which means that the transverse matching conditions ($\sigma_z < \lambda_p/2$) will be more difficult to reach, because it will be much more challenging to produce bunches with a shorter duration. On the other hand with a higher emittance we have more relaxed matching conditions, but a high emittances means a shorter β function (and so a shorter Rayleigh length), resulting in a rapid growth of the electron beam spot-size exiting the plasma.

In order to achieve the matching conditions in the COMB experiment, during this thesis work, S2E simulation of the SPARC_LAB linac up to the COMB interaction chamber have been performed, searching for an appropriate scheme of the focusing magnetic elements in the beam line and inserting two new triplets of quadrupoles before plasma.

The impact of the results inserting in the beam line this two new triplets of quadrupoles and using the solenoid around S2-band with a proper field were presented. With this configuration we will have the smallest spot size, before the plasma capillary, achievable at SPARC_LAB during the COMB experiment with a witness bunch of 25 pC.

The found spot size during the simulations doesn't match perfectly with the matching conditions, but has a sufficient small size to be injected in the plasma channel.

In the final results a more appreciable spot size was presented, obtained with the same magnetic configuration of the two triplets varying only the field of the solenoid around S2-band, in this configuration the beam waist moves along z, and is below 1 cm after the plasma start. This configuration will take profit of the focus effect of the plasma to be properly captured. The focus effect of the plasma in fact, reducing the bunch spot size, will bring closer to the matching conditions.

It has been presented a simulation with the GPT code in which the plasma, with a density of $n_0 = 10^{16} \text{ cm}^{-3}$ and a plasma length $\lambda_p \approx 330 \mu\text{m}$ ($\omega_p \approx 1 \text{ THz}$), has been modeled as a THz RF cavity, just to have some insight about the beam dynamics in such a short wavelength accelerating field. With this simulation the gradients of three quadrupoles after the plasma have been evaluated, in order to capture the bunch after the plasma acceleration.

In summary this thesis evaluated the focusing elements on the beam line to achieve, in the SPARC_LAB linac, the best spot size for the COMB plasma acceleration experiment.

Bibliography

- [1] D. Alesini, S. Bertolucci, et al. The SPARC project: a high-brightness electron beam source at Inf to drive a sase-fel experiment. *Nuclear Instruments and Methods in Physics Research Section A: Accelerators, Spectrometers, Detectors and Associated Equipment*, 507(1–2):345 – 349, 2003.
- [2] D. Alesini, S. Bertolucci, et al. The sparx sase-fel projects. *Laser and Particle Beams*, 22:341–350, 6 2004.
- [3] P. Valente, F. Anelli, et al. Development of a multi-GeV spectrometer for laser–plasma experiment at flame. *Nuclear Instruments and Methods in Physics Research Section A: Accelerators, Spectrometers, Detectors and Associated Equipment*, 653(1):42 – 46, 2011.
- [4] V. Petrillo, M.P. Anania, et al. Observation of time-domain modulation of free-electron-laser pulses by multipeaked electron-energy spectrum. *Physical Review Letters*, 111(11):114802, 2013.
- [5] L. Giannessi, A. Bacci, et al. Self-amplified spontaneous emission free electron laser with an energy-chirped electron beam and undulator tapering. *Physical review letters*, 106(14):144801, 2011.
- [6] L. Giannessi, D. Alesini, et al. Self-amplified spontaneous emission for a single pass free-electron laser. *Phys. Rev. ST Accel. Beams*, 14:060712, Jun 2011.
- [7] D. Alesini, S. Guiducci, et al. Proceedings of the 10th european particle accelerator conference, edinburgh, scotland, 2006.

- [8] A. Bacci, D. Alesini, et al. Electron linac design to drive bright compton back-scattering gamma-ray sources. *Journal of Applied Physics*, 113(19):194508–194508, 2013.
- [9] E. Chiadroni, A. Bacci, et al. The sparc linear accelerator based terahertz source. *Applied Physics Letters*, 102:094101, 2013.
- [10] E. Chiadroni, M. Bellaveglia, et al. Characterization of the thz radiation source at the Frascati linear accelerator. *Review of Scientific Instruments*, 84(2):022703, 2013.
- [11] A. Mostacci, M. Bellaveglia, et al. Chromatic effects in quadrupole scan emittance measurements. *Phys. Rev. ST Accel. Beams*, 15:082802, Aug 2012.
- [12] D. Filippetto, M. Bellaveglia, et al. Phase space analysis of velocity bunched beams. *Phys. Rev. ST Accel. Beams*, 14:092804, Sep 2011.
- [13] L. Serafini and J. B. Rosenzweig. Envelope analysis of intense relativistic quasilaminar beams in rf photoinjectors: a theory of emittance compensation. *Physical Review E*, 55(6):7565, 1997.
- [14] A. Cianchi, D. Alesini, et al. High brightness electron beam emittance evolution measurements in an rf photoinjector. *Phys. Rev. ST Accel. Beams*, 11:032801, Mar 2008.
- [15] Martin Reiser. Theory and design of charged particle beams. *John Wiley & Sons*, 2008.
- [16] M. Ferrario et al. Slac-pub-8400, 2000.
- [17] M. Ferrario, D. Alesini, et al. Direct measurement of the double emittance minimum in the beam dynamics of the sparc high-

- brightness photoinjector. *Physical review letters*, 99(23):234801, 2007.
- [18] A.R. Rossi, WEEPPB002, These Proceedings.
- [19] S. Cialdi, M. Petrarca, et al. High-power third-harmonic flat pulse laser generation. *Optics letters*, 31(19):2885–2887, 2006.
- [20] W.S. Graves, L.F. Di Mauro, et al. Measurement of thermal emittance for a copper photocathode. In *Particle Accelerator Conference, 2001. PAC 2001. Proceedings of the 2001*, volume 3, pages 2227–2229 vol.3, 2001.
- [21] T. Alesini et al., JINST, 8, P05004, 2013.
- [22] A. Mostacci et al., TUPPD055, These Proceedings.
- [23] P. Muggli, Proc. of PAC 2009, Vancouver, Canada.
- [24] E. Chiadroni et al., Proceedings of IPAC 2010, TUOARA03, Kyoto, 2010.
- [25] M.S. Sherwin et al., Opportunities in THz Science, Report of a DOE-NSF-NIH, Workshop (2004).
- [26] E. Chiadroni et al., Rev. Sci. Instr. 84 (2013) 022703.
- [27] A.Lindblad, S.Svensson and K.Tiedtke. A compendium on beam transport and beam diagnostic methods for Free Electron Lasers. Deutshes Electronen Synchrotron DESY (2011).
- [28] M. Ferrario et al., Nucl. Instr. Meth. A 637 (1) (May 2011) S43–S46.
- [29] A. Mostacci et al., TUPPD055, These Proceedings.
- [30] P. Muggli, Proc. of PAC 2009, Vancouver, Canada.
- [31] P. Tomassini, Private Communication

- [32] B. Cross et al., *Phys. Rev. E* 65 (2002) 026405
- [33] P. Antici et al., *J. Appl. Phys.* 112 (2012) 044902
- [34] A.R. Rossi, WEEPPB002, These Proceedings
- [35] W. K. H. Panofsky and M. Breidenbach. Accelerators and detectors. *Review of Modern Physics*, 1999.
- [36] W. Ackermann, G. Asova, et al. Operation of a free-electron laser from the extreme ultraviolet to the water window. *Nature photonics*, 1(6):336–342, 2007.
- [37] DESY. http://hasylab.desy.de/images/content/e208/e209/index_eng.html, 2007.
- [38] W Wuensch, C Achard, et al. Demonstration of high-gradient acceleration. In *Particle Accelerator Conference, 2003. PAC 2003. Proceedings of the*, volume 1, pages 495–497. IEEE, 2003.
- [39] Elizabeth Clements. Clic. the compact linear collider.
- [40] David P. Pritzkau and Robert H. Siemann. Experimental study of rf pulsed heating on oxygen free electronic copper. *Phys. Rev. ST Accel. Beams*, 5:112002, Nov 2002.
- [41] S. Humphries, Charged particle beams, *Wiley*, New York, 2002.
- [42] M. Reiser, Theory and Design of Charged Particle Beams, *Wiley*, New York, 1994.
- [43] T. Wangler, Principles of RF linear accelerators, *Wiley*, New York, 1998
- [44] F. J. Sacherer, F. J., *IEEE Trans. Nucl. Sci.* NS-18, 1105 (1971).

- [45] J. B. Rosenzweig, *Fundamentals of beam physics*, Oxford University Press, New York, 2004.
- [46] M. Ferrario et al., *Int. Journal of Modern Physics A*, Vol 22, No. 23, 4214 (2007).
- [47] K.L.F. Bane et al., *Phys. Rev. ST Accel. Beams* 12, 030704, 2009.
- [48] B. Aune and R.H. Miller, Report No. SLAC-PUB 2393, 1979.
- [49] B.E. Carlsten, *Nucl. Instrum. Methods Phys. Res., Sect. A* 285, 313, 1989.
- [50] L. Serafini and M. Ferrario, *AIP Conf. Proc.* 581, 87, 2001.
- [51] M.Ferrario, D.Alesini, et al., Experimental Demonstration of Emittance Compensation with Velocity Bunching. *Physical Review Letter* 104. 5 (2010): 054801.
- [52] L. Serafini and J.B. Rosenzweig, *Phys. Rev. E* 55, 7565 (1997).
- [53] C. Ronsivalle et al., in *Proceedings of EPAC 02*, Paris (EPS-AG, Geneva, 2002).
- [54] J.B. Rosenzweig and L. Serafini, *Phys. Rev. E* 49, 1599 (1994).
- [55] M. Ferrario et al., *Nucl. Instr. Meth. A* 637 (1) (May 2011) S43–S46.
- [56] A. Mostacci et al., TUPPD055, These Proceedings.
- [57] P. Muggli, *Proc. of PAC 2009*, Vancouver, Canada.
- [58] E. Chiadroni et al., *J. Phys: Conf. Ser.* 357 (2012) 012034.
- [59] A. Bacci et al., *Proceedings of FEL Conference 2011*, Shanghai, China, 2011.

- [60] Y. B. Fainberg, V. A. Balakirev, et al. Wake field excitation in plasma by a train of relativistic electron bunches. *Plasma Physics Reports*, 20:606–612, July 1994.
- [61] Chandrashekar Joshi. Plasma accelerators. *Scientific American*, 294(2):40–47, 2006.
- [62] Efthymios Kallos. Plasma Wakefield accelerators using multiple electron bunches. PhD thesis, *Faculty of the Graduate School, University of Southern California*, August 2008.
- [63] T. Tajima and J. M. Dawson. Laser electron accelerator. *Physical Review Letters*, 43:267, July 1979.
- [64] T. Katsouleas and J. M. Dawson. Unlimited electron acceleration in laser-driven plasma waves. *Physical Review Letters*, 51:392–395, August 1983.
- [65] C. Joshi, W. B. Mori, et al. Ultrahigh gradient particle acceleration by intense laser-driven plasma density waves. *Nature*, 311:525–529, October 1984.
- [66] P. Chen, J. M. Dawson, et al. Acceleration of electrons by the interaction of a bunched electron beam with a plasma. *Physical Review Letters*, 54:693–696, February 1985.
- [67] P. Maine, D. Strickland, et al. Chirped pulse amplification: Present and future. *NASA STI/Recon Technical Report N*, 89:14434, 1988.
- [68] P. Maine, D. Strickland, et al. Tabletop terawatt laser by chirped pulse amplification. In E. M. Campbell and H. Baldis, editors, *Society of Photo-Optical Instrumentation Engineers (SPIE) Conference Series*,

volume 913 of *Society of Photo-Optical Instrumentation Engineers (SPIE) Conference Series*, pages 140–146, January 1988.

- [69] P. Maine, D. Strickland, et al. Generation of ultrahigh peak power pulses by chirped pulse amplification. *IEEE Journal of Quantum Electronics*, 24:398–403, February 1988.
- [70] E. Esarey, P. Sprangle, et al. Overview of plasma-based accelerator concepts. *IEEE Transactions on Plasma Science*, 24:252–288, April 1996.
- [71] K. Nakajima, T. Kawakubo, et al. Proof-of-principle experiments of laser wakefield acceleration using a 1 ps 10 TW Nd:glass laser. In *American Institute of Physics Conference Series*, volume 335 of *American Institute of Physics Conference Series*, pages 145–155, June 1995.
- [72] Max Born Institut. <http://www.mbi-berlin.de/en/research/projects/2.1/topics/UP2/index.html>, 2012.
- [73] E. Esarey, C. B. Schroeder, et al. Physics of laser-driven plasma-based electron accelerators. *Reviews of Modern Physics*, 81:1229–1285, July 2009.
- [74] J. B. Rosenzweig, D. B. Cline, et al. Experimental observation of plasma wake-field acceleration. *Physical Review Letters*, 61:98–101, July 1988.
- [75] W. Lu, C. Huang, et al. Limits of linear plasma wakefield theory for electron or positron beam. *Phys. Plasmas*, 12, 063101, 2005.
- [76] W. Lu, C. Huang, et al. A nonlinear theory for multidimensional relativistic plasma wave wakefields. *Phys. Plasmas*, 13, 056709, 2006.

- [77] P. Londrillo, C. Gatti, and M. Ferrario. Numerical investigation of beam-driven PWFA in quasi-nonlinear regime. *Nuclear Instruments and Methods in Physics Research Section A: Accelerators, Spectrometers, Detectors and Associated Equipment* 740 (2014): 236-241.
- [78] J.B. Rosenzweig, N. Barov, et al., Energy loss of a high charge bunched electron beam in plasma: Simulations, scaling, and accelerating wakefields. *Physical Review Special Topics*, 7, 061302, 2004.
- [79] J.B. Rosenzweig, G. Andonian, et al., Plasma Wakefield in the Quasi nonlinear Regime. Advanced Accelerator Concepts, 14th Advanced Accelerator Concepts Workshop. *AIP Publishing*, 2010. p. 500-504.
- [80] M.Ferrario, Accelerator physics: basic principles on beam focusing and transport, SPARC-BD-12/01, 2012.
- [81] E. Esarey et al., *Physics of laser-driven plasma-based electron accelerators*, Rev. of modern physics, V. 81, July–September 2009.
- [82] C. Joshi and w. B. Mori, *The status and evolution of plasma wakefield particle accelerators*, Phil. Trans. R. Soc. A 2006 364, 577-585.
- [83] J. B. Rosenzweig et al., Phys. Rev. A, V. 44, N. 10, 1991.
- [84] P. Muggli and M. J. Hogan, Review of high-energy plasma wakefield experiments, *C. R. Physique*, 10, 116–129, 2009.
- [85] W. Lu et al., PRL 96, 165002 (2006).
- [86] Klaus Halbach and RF Holsinger. *Superfish-a computer program for evaluation of rf cavities with cylindrical symmetry. part. Accel.*, 7(LBL5040):213–222, 1976.

Ringraziamenti

Ho iniziato a lavorare su questa tesi con una scarsa conoscenza degli argomenti che avrei dovuto trattare e con un certa curiosità nei confronti di quella figura che all'università mi avevano insegnato a chiamare "macchinista". Oggi che concludo questo lavoro sono tanto affascinato da questa branca della fisica da iniziare il giorno dopo la laurea un dottorato di ricerca in fisica degli acceleratori. L'esperienza di questi mesi presso la facility SPARC_LAB è stata molto faticosa, ma estremamente formativa. L'ambiente in cui mi sono inserito è composto da persone dotate di una grande competenza e con una dedizione totale alla ricerca, ma al tempo stesso capaci di creare un ambiente di lavoro in cui regna la disponibilità e la cordialità.

Desidero innanzitutto ringraziare il Dr. Massimo Ferrario che mi ha dato la possibilità di entrare a far parte del suo gruppo di ricerca e mi ha seguito per tutti questi mesi con grandissima dedizione. Gli sono immensamente grato per tutto il tempo che mi ha dedicato, soprattutto per i chiarimenti teorici sulla dinamica del fascio e sui plasmi. A lui devo la formazione e la passione che ho acquisito in questi mesi per la materia.

Ringrazio il Prof. Faccini per la grande disponibilità e la cortesia che mi ha dimostrato ed anche per aver contribuito a risolvere rapidamente i problemi burocratici che si sono presentati.

Ringrazio di cuore anche Riccardo Pompili per avermi aiutato nell'apprendimento del software GPT, e per avermi aiutato nei numerosi problemi che si sono creati durante questo lavoro di tesi; senza di lui molte delle cose scritte in queste pagine non ci sarebbero.

Esprimo una profonda gratitudine a Maria Pia Anania per i chiarimenti su GPT e sui plasmi, per le correzioni di inglese, e non ultima per la sua grande simpatia.

Ringrazio anche tutti i vicini di stanza, alcuni dei quali diventati veri e propri amici, che con semplici chiacchierate hanno contribuito a chiarirmi le idee secondo le loro competenze: Alessandro, Marco, Niko, Fabio, Enrica, Cristina, Stefano, Anna e Francesco.

Sono grato agli amici di sempre che mi sono stati accanto in questi anni, soprattutto nei momenti meno felici: Nicola, Edoardo, Gianluca, Marco, Eleonora, Gian Marco, Alessandro e Lorenzo.

Grazie anche a Elena, Davide, Simona e Luigi per la vostra amicizia, perché ci siete sempre.

Non posso dimenticare Loretta e Paola con cui ho condiviso gli ultimi sforzi all'università, conserverò sempre un bel ricordo di quei momenti.

Ringrazio la mia famiglia a cui devo tutto e per dire cosa sia questo tutto non basterebbero le pagine di questa tesi.

Benedetta dovresti essere stata la prima della lista, solo tu sai quanto mi sia costato questo cammino universitario, e tu ci sei sempre stata più di ogni altro. Grazie. Non basterà una vita per dirtelo.

Nonna Luciana avrei voluto ringraziarti di persona, per tutto quello che sei stata e mi hai dato. Da quando ho iniziato l'asilo mi sei sempre stata vicino, avrei voluto farti leggere queste righe tornando a casa il giorno della mia laurea, ma sapendo che le puoi vedere comunque dall'alto, ti dedico questa tesi.